

PROCESSING AND CHARACTERIZATION OF
TANTALUM-HAFNIUM CARBIDES

by

BRADFORD CHRISTOPHER SCHULZ

GREGORY B. THOMPSON, COMMITTEE CHAIR
DANIEL BUTTS
GARRY WARREN
PATRICK KUNG

A THESIS

Submitted in partial fulfillment of the requirements for the degree
of Master of Science in the Department of
Metallurgical and Materials Engineering
in the Graduate School of
The University of Alabama

TUSCALOOSA, ALABAMA

2011

Copyright Bradford Christopher Schulz 2011
ALL RIGHTS RESERVED

ABSTRACT

A series of $(\text{TaC})_{100-x}(\text{HfC})_x$ specimens were manufactured by two different processing techniques and studied to determine the effect of hafnium content on the tantalum carbide microstructure. The first set of $(\text{TaC})_{100-x}(\text{HfC})_x$ specimens, where X is 0.3, 3.0, 16.5, and 19.8 at.% HfC, were fabricated by the vacuum plasma spraying process (VPS) with subsequent sintering and hot isostatic pressing (HIPing) to homogenize the microstructure. The second set of specimens of $(\text{TaC})_{100-x}(\text{HfC})_x$, where X is 5.8, 10.7, 17.6, and 25.0 at.% HfC, were fabricated from arc melted powder blends (AMPP) of these compositions with subsequent hot isostatic pressing and spark plasma sintering (SPS). It was found that as HfC content increased, the grain size was reduced, the porosity fraction increased, and volume fraction of TaC, Ta_2C and Ta_4C_3 changed. The reduction of grain size with increasing HfC content has been explained by the system being driven further into a compositionally lower melting temperature phase field upon solidification of either the powders in the VPS plasma plume or the initial state of the arc melted powders for AMPP-SPS. This increase in liquid fraction caused greater under-cooling and the formation of more nucleation sites that lead to a finer grain size. The changing volume fraction of $(\text{TaC})_{100-x}(\text{HfC})_x$ and sub-stoichiometric tantalum carbide phases has been explained through the unequal loss of constituent species during processing.

The addition of HfC content improved the micro hardness values as tested by Knoop indentation at room temperature. It was observed that the micro hardness values increased with respect to increasing HfC content. The addition of HfC content was found to improve the

oxidation resistance at 1000°C. The oxide scale was composed primarily of orthogonal and hexagonal Ta₂O₅ and monoclinic HfO₂ phases.

LIST OF ABBREVIATIONS AND SYMBOLS

AMPP	Arc melt powder process
at.%	Atomic percent
<i>bcc</i>	Body centered cubic
C_p	Heat capacity
°C	Celsius
Cub	Cubic
C:M	Carbon-to-metal ratio
CTE	Coefficient of thermal expansion
ρ	Density
DBTT	Ductile-to-brittle transition temperature
E	Young's Modulus
EBSD	Electron backscattered diffraction
EDS	Energy dispersive spectroscopy
<i>et al.</i>	And others
eV	Electron volts
<i>fcc</i>	Face centered cubic
FIB	Focused ion beam
ΔG	Free energy of formation
GPa	Giga-Pascal
ΔH_f	Enthalpy of formation

HAADF	High angle annular dark field
<i>hcp</i>	Hexagonal close packed
Hex	Hexagonal
HfC	Hafnium carbide
HIP	Hot isostatic pressing
HK	Knoop hardness
I	Current, in Amperes
J	Joules
<i>k</i>	Thermal conductivity
K	Kelvins
keV	Kilo-electron volts
kJ	Kilo-Joules
m	Meters
M-C	Metal-carbon bonding
M-M	Metal-metal bonding
mol	Moles
ROI	Region of interest
σ_y	Yield stress
SAED	Selected area electron diffraction
SEM	Scanning electron microscope
SPS	Spark plasma sintering
STEM	Scanning transmission electron microscope
TaC	Tantalum carbide

TEM	Transmission electron microscope
T _m	Melting temperature
UHTC	Ultra high temperature ceramic
VPS	Vacuum plasma spraying
W	Watts
XRD	X-ray diffraction

ACKNOWLEDGMENTS

I am proud to have the opportunity to thank my colleagues, friends, family, and faculty members who have helped me along with my career and this research project. First and foremost, I would like to thank my advisor Gregory Thompson, the chairman of this thesis, for sharing his technical and research expertise as well as wisdom and guidance in materials science and in molding my career. I would also like to thank my committee members, Daniel Butts, Patrick Kung, and Garry Warren for their invaluable input, questions, and support for my thesis and my overall academic progress. Additionally, I would like to thank Daniel Butts with Plasma Processing, LLC, Larry Matson with Air Force Research Lab, and Lee Heedong with United Energy System, Inc. for providing bulk samples of the TaC-HfC composition samples used in this research. I would like to thank Billie Wang for his contributions in the interface tracking model. I would also like to thank my mentor, Robb Morris, for his guidance and training. Additionally, I would also like to thank Alex Blackwell for his assistance as an undergraduate research assistant. A majority of this work has been financially supported by the Missile Defense Agency under grants MDA Phase II SBIR contract No. W9113M-09-C-0099 and contract No. HQ0006-10-C-7394.

Lastly, I would like to once again emphasize that this research is possible due to the support from my family, friends, and fellow graduate students.

CONTENTS

ABSTRACT.....	II
LIST OF ABBREVIATIONS AND SYMBOLS	IV
ACKNOWLEDGMENTS	VII
LIST OF TABLES	X
LIST OF FIGURES	XI
CHAPTER 1 INTRODUCTION	1
1.1 MOTIVATION.....	1
1.1.1 Ultra High Temperature Ceramics	2
1.1.2 UHTC Design Challenges	3
1.2 ADDITIVES IN UHTCs.....	4
1.3 TANTALUM-HAFNIUM-CARBIDE SYSTEM	5
1.3.1 The Tantalum-Carbon System.....	5
1.3.2 The Hafnium-Carbon System.....	9
1.3.3 Mixing Tantalum-Hafnium-Carbon	9
1.4 UHTC PROCESSING	13
1.4.1 ‘Top-Down’ Processing.....	13
1.4.2 ‘Bottom-Up’ Processing.....	13
CHAPTER 2 EXPERIMENTAL.....	15
2.1 VACUUM PLASMA SPRAY PROCESSING.....	15
2.2 ARC-MELT POWDER PROCESSING.....	16
2.3 GENERAL SPECIMEN PREPARATION	16
2.4 SPECIMEN CHARACTERIZATION	16
2.4.1 FEI Quanta 3D FIB.....	16
2.4.2 Bruker D8 GADDS	17
2.4.3 FEI F20 Tecnai	17

2.5	KNOOP MICRO-INDENTATION HARDNESS MEASUREMENTS.....	18
2.6	OXIDATION HEAT TREATMENTS	18
CHAPTER 3 MICROSTRUCTURE AND PHASE FORMATION.....		20
3.1	VPS AND AMPP-SPS PROCESSED $Ta_{1-x}Hf_xC$ MICROSTRUCTURE AND PHASE RESULTS	20
3.1.1	Microstructure and Grain Size.....	21
3.1.2	Porosity.....	25
3.1.3	26
3.1.4	Phase Characterization	27
3.2	VPS AND AMPP-SPS $(TAC)_{100-x}(HfC)_x$ MICROSTRUCTURE AND PHASE DISCUSSION...	30
3.2.1	Grain Size and Porosity Analysis	30
3.2.2	Phase Formation	35
CHAPTER 4 FRACTURE AND OXIDATION BEHAVIOR.....		46
4.1	VPS AND AMPP-SPS PROCESSED $(TAC)_{100-x}(HfC)_x$ INDENTATION RESULTS	46
4.1.1	Indent Behavior	46
4.1.2	Fracture Behavior Analysis	49
4.2	AMPP-SPS PROCESSED $Ta_{1-x}Hf_xC$ OXIDATION RESULTS	51
4.2.1	Oxide Phase Characterization.....	51
4.2.2	Oxidation Behavior.....	53
4.2.3	Oxidation Analysis	58
CHAPTER 5 CONCLUSION.....		60
5.1	MAJOR FINDINGS	60
5.2	FUTURE WORK.....	61
CHAPTER 6 REFERENCES		62
CHAPTER 7 APPENDIX.....		69

LIST OF TABLES

Table 1-1 Summary of structural, physical, transport, and thermodynamic properties of major UHTC carbides. [6-10]	2
Table 3-1 Initial volume phase %, porosity %, mean grain diameter, and estimated carbon loss during VPS processing of tantalum-hafnium carbides with respect to at.% HfC.....	20
Table 3-2 Initial volume phase %, porosity %, mean grain diameter, and estimated carbon loss during AMPP-SPS processing of tantalum-hafnium carbides with respect to at.% HfC.	21
Table 3-3 Phase formation analysis for the 19.8 at.% HfC specimen based on phase diagram information at 1850°C [82] for a composition with 40 at.% carbon. The tie lines in Figure 3-13(b) for carbon (dashed line) and hafnium + carbon (solid line) loss were used to estimate phase %. See Appendix 7-5 for sample calculation.....	39
Table 4-1 Knoop indentation results for 200g load for the VPS processed specimens.	46
Table 4-2 Knoop indentation results for 200g load for the VPS processed specimens.	46
Table 4-3 Oxidation results for the AMPP-SPS processed specimens. Oxidation treatment conducted at 1000°C for 30 min.	51

LIST OF FIGURES

Figure 1-1 The tantalum-carbon binary phase diagram. [46]	7
Figure 1-2 The (a) B1 rock-salt structure γ -TaC [47], the (b) rhombohedral ζ -Ta ₄ C ₃ [48] and (c) β -Ta ₂ C [49] crystal structure. [29]	7
Figure 1-3 Morphology changes in tantalum carbide microstructures based on carbon content for (a) 56Ta44C, (b) 58Ta42C, (c) 60Ta40C, (d) 64Ta36C, and (e) 68Ta32C. [29]	8
Figure 1-4 The crystallographic structures of Ta ₂ O ₅ : Triclinic (a), Monoclinic (b), Orthorhombic (c), and Hexagonal (d). [38-41]	8
Figure 1-5 The B1 rock-salt structure HfC [62].....	11
Figure 1-6 The hafnium-carbon binary phase diagram. [50]	11
Figure 1-7 The crystallographic structures of HfO ₂ : Monoclinic (a), Orthorhombic (b), and Tetragonal (c). [53-55].....	12
Figure 2-1 Knoop indentation schematic drawings. [79].....	19
Figure 2-2 Schematic drawing of heat treatments for oxidation analysis.....	19
Figure 3-1 Representative EBSD images of (a) 0.3 at.% HfC, (b) 3.0 at.% HfC, (c) 16.5, and (d) 19.8 at.% HfC VPS processed specimens. The black regions represent pores.....	22
Figure 3-2 Representative EBSD images of (a) 5.7 at.% HfC, (b) 10.7 at.% HfC, (c) 17.6 at.% HfC, and (d) 25.0 at.% HfC AMPP-SPS processed specimens. The black regions represent pores.	22
Figure 3-3 Mean grain diameter plotted against at.% HfC taken from Figure 3-1(a-d) for VPS processed specimens.	23
Figure 3-4 Mean grain diameter plotted against at.% HfC taken from images Figure 3-2(a-d) for AMPP-SPS processed specimens.	23
Figure 3-5 SEM-FIB ion contrast images of the (a) 0.3, (b) 3.0, (c) 16.5, and (d) 19.8 at.% VPS processed microstructures.....	24
Figure 3-6 SEM-FIB ion contrast images of bulk regions for the (a) 5.8, (b) 10.7, (c) 17.6, (d) and 25.0 at.% AMPP-SPS processed specimens.	24

Figure 3-7 Dark field images from TEM for the 19.8 at.% specimen for <011>, <112>, and <011> orientations. The white arrows indicate invisible conditions while the black arrows indicate visible conditions.....	26
Figure 3-8 XRD results from the 0.3, 3.0, 16.5 and 19.8 at.% HfC VPS processed specimens. Each spectra revealed the phases TaC, Ta ₂ C, Ta ₄ C ₃ at various diffracted intensities.	28
Figure 3-9 XRD results from the 5.8, 10.7, 17.6 and 25.0 at.% HfC non-oxidized AMPP-SPS specimens. Each spectra revealed the phases TaC and Ta ₂ C at various diffracted intensities.	28
Figure 3-10 Lattice parameters with respect to at.% HfC for the VPS specimens (a) TaC cubic lattice parameter <i>a</i> -, (b) Ta ₂ C hexagonal lattice parameter <i>a</i> - and <i>c</i> -, and (c) Ta ₄ C ₃ rhombedral lattice parameter <i>a</i> - and <i>c</i> -.....	29
Figure 3-11 Ternary phase diagram for tantalum-hafnium-carbon at a) 1000°C, b) 1500°C, c) 1850°C, and d) 2500°C. [82-85]	31
Figure 3-12 Interface tracking model results (a) microstructure grain size as <i>T_m</i> decreases from 4000 to 1500°C where T ₁ > T ₂ > T ₃ > T ₄ > T ₅ > T ₆ in the images and T represents temperature (b) Time evolution for <i>T_m</i> 3000°C where t ₁ < t ₂ < t ₃ < t ₄ < t ₅ < t ₆ < t ₇ < t ₈ in the images and t represents time.	34
Figure 3-13 Ternary phase diagram of Ta-Hf-C at (a) 2500°C [83] with dashed lines indicating a continual carbon loss for 3.0 at.% HfC and 19.8 at.% HfC. Arrow 1 shows carbon loss for 3.0 at.% HfC. Arrow 2 points in the direction of phase field stability with an increase from 3.0 at.% to 19.8 at.% HfC. Arrow 3 shows carbon loss for 19.8 at.% HfC. (b) The region of interest on the 1850°C [82] phase diagram is magnified; the carbon loss for 3.0 at.% (dotted line) and 19.8 at.% HfC (dashed line) are marked. The fine dotted line represents the tie-line between the TaC+HfC phase field and Ta ₂ C for Point A, located approximately at 13 at.% carbon loss. The solid line represents equal loss of carbon and hafnium for the 19.8 at.% HfC specimen.	37
Figure 3-14 The vapor pressures for carbon which is highlighted. [87].....	40
Figure 3-15 The vapor pressures for hafnium which is highlighted. [87]	41
Figure 3-16 The vapor pressures for tantalum which is highlighted. [87].....	42
Figure 3-17 Effects of equivalent hafnium and carbon mobility during processing. The results are represented by a 2-D topography graph where the x-axis is initial (TaC) _{100-x} (HfC) _x composition with respect to HfC content, the y-axis is hafnium and carbon elemental % loss, and the z-axis is the carbon-to-metal ratio after processing represented by contour lines. The approximation of 13 % elemental loss is represented by the bold line.....	44

Figure 4-1 SEM electron imaging of indent behavior for VPS processed (a) 0.3, (b) 3.0, (c) 16.5, and (d) 19.8 at.% HfC specimens.	48
Figure 4-2 SEM electron imaging of indent behavior for AMPP-SPS processed (a) 5.8, (b) 10.7, (c) 17.6, and (d) 25.0 at.% HfC specimens.	48
Figure 4-3 Plot of initial HfC content vs. mean grain diameter (μm) and Knoop value conducted at 200g for the VPS and AMPP-SPS processed specimens.	50
Figure 4-4 Plot of HfC content vs. Ta_4C_3 phase volume % for the VPS and AMPP-SPS processed specimens.	50
Figure 4-5 XRD results (a) from the AMPP-SPS processed 5.8, 10.7, 17.6 and 25.0 at.% HfC oxidized specimens at 1000°C for 30 min. Each spectra revealed the phases (b) Ta_2O_5 and HfO_2 at various diffracted intensities and crystallographic structures. Underlined/highlighted phases indicate closest in d-spacing.	52
Figure 4-6 SEM-FIB ion contrast images of oxide, heat treated at 1000°C for 30 min, and bulk regions for the (a) 5.8, (b) 10.7, (c) 17.6, (d) and 25.0 at.% specimens.	54
Figure 4-7 SEM-FIB ion contrast images showing the oxide scale length, heat treated at 1000°C for 30 min, for the (a) 5.8, (b) 10.7, (c) 17.6, (d) and 25.0 at.% specimens.	54
Figure 4-8 Representative SEM images of the specimens; 5.7 at.% HfC (a), 10.7 at.% HfC (b), 17.6 at.% HfC (c), and 25.0 at.% HfC (d) oxide scale transition, heat treated at 1000°C for 30 min. Composite image (e) of bulk to oxide transition for the 25.0 at.% HfC specimen.	55
Figure 4-9 SEM-EDS (a) results of C(K)/O(K) vs. position from carbide to oxide scale. Representative STEM-HAADF composite images of 25.0 at.% HfC (b) from carbide to oxide interlayer with EDS mapped region and (c) from carbide to oxide.	57
Appendix 7-1 Example XRD identification template for the Ta-C system. CaRIne Crystallographic software was used.	69
Appendix 7-2 Lattice parameter example calculations for 19.8 at.% specimen. The peak data gathered by the XRD machine was analyzed by Origins software. Double peaks were deconvoluted. Example for TaC lattice parameter a- and Ta_2C lattice parameter a- and c- calculations are shown.	70
Appendix 7-3 Phase volume % example calculation for 19.8 at.% specimen. The peak data gathered by the XRD machine was analyzed by Origins software. Double peaks were deconvoluted. The most intense peak for each phase [111], [101], and [107] were used to calculate	

the phase %. The phase volume % was based off the area under the intense peak for each phase. 71

Appendix 7-4 Example porosity calculation. A generic SEM image would be analyzed with imaging software. A R-G-B color scale threshold was applied so that the dark regions (pores) were highlighted. The area of the pores was calculated by the software. The porosity % was calculated by the equation given. 72

Appendix 7-5 Sample at.% loss of carbon for the given phase diagram at 1850°C. Tie lines were measured in the region of interest for each specimen and the TaC boundary was adjusted for at.% of carbon at the tie line interface. These adjusted Ta and C values combined with phase % values produced a Ta:C ratio. This Ta:C ratio was used to determine the resulting overall at.% C loss for the specimen. 73

Appendix 7-6 Example Knoop indentation measurement. The length of the indentation at specified loads would correlate with a HK value. 74

Appendix 7-7 Example oxide mass % change and oxide scale thickness calculation. The mass % change was based on heat treated specimens loaded in ceramic boats which were normalized in the calculations. The mass of the boat and sample was measured before and after heat treatments to produce the mass % change. SEM images were used to measure the scale thickness. An average of 3 runs for both the mass change and scale thickness were conducted. 75

Chapter 1 Introduction

1.1 Motivation

Materials engineering seeks to understand the relationship between processing, properties, and structure in order to improve engineering designs and applications. This is accomplished by studying materials at all length scales of structure, nano to micro to macro. Bridging the gaps between processing-properties and properties-structure is conducted via the characterization tools and techniques incorporated with materials microscopy. By studying the processing-properties-microstructure interrelationship, material scientists will be able to engineer specific microstructures that result in the ability to design desired properties. This work studied the processing-properties-microstructure behavior of an ultra-high temperature ceramic (UHTC) system, Ta(Hf)C, and will primarily focus on the interrelationship of HfC content on the tantalum carbide microstructure. The hardness and oxidation properties were also measured.

The UHTC family of materials is characterized by high melting points, chemical inertness, high hardness, and moderate oxidation resistance [1]. These refractory compounds consist of ceramic carbides, borides, and nitrides mainly from the transition metal groups IV and V. These materials nominally have melting temperatures in excess of 3000°C [2]. UHTCs are ideally suited materials to be used in extreme environmental conditions. According to Wuchina and Fahrenholtz, extreme environmental conditions are best described by the parameters associated with the following applications: handling of molten metals, electrodes for electric arc furnaces, and aerospace applications [3].

Prior research and knowledge in UHTCs has primarily focused on the processing-property relationship [1-3]; however, there is not extensive literature on the structure-property or processing-structure relationship in particular to hafnium carbide additions to tantalum carbides. Thus there is a need for a systemic research program on materials to address this microstructure relationship in this UHTC.

1.1.1 Ultra High Temperature Ceramics

It is believed that strong atomic bonding is the reason UHTCs have high melting points, moduli and hardness [1,4]. The UHTCs typically have either: ionic or covalent bonds. This work focuses primarily on ceramic carbides, TaC and HfC, which has strong covalent bonding with strong carbon networks. The atomic metal-nonmetal bonding is based on the interaction between the carbon's $2s$ - and $2p$ -orbitals with the metal d -orbitals [4]. A review on the quantum-chemical relations in binary carbides by Gubanov *et al.* revealed that the attraction between atoms in cubic carbides is mainly due to σ -hybridization of metal d -orbitals and metalloid $2p$ -orbitals; moreover, bonding-property relationships are mainly dependent on metal-nonmetal bonding versus metal-metal bonding [5]. The large negative free energies of formation, ΔG found in Table 1-1, give UHTCs good chemical and thermal stability in ultra conditions.

Table 1-1 Summary of structural, physical, transport, and thermodynamic properties of major UHTC carbides. [6-10]

Property	ZrC	HfC	TaC
Crystal Space Group	Cub	Cub	Cub
ρ (g/cm ³)	6.7	12.2	14.5
T_m (°C)	3532	3890	3880
E (GPa)	489	510	560
Hardness (GPa)	24	23	25
CTE (10 ⁻⁶ /K ⁻¹)	6.6	6.3	7.2
C_p at 25°C (Jmol ⁻¹ K ⁻¹)	38	60.4	35.9
K at 25°C (Wm ⁻¹ K ⁻¹)	20	22	22
ΔH_f at 25°C (kJ)	-197	-208	-144
ΔG at 25°C (kJ)	-193	-205	-143

1.1.2 UHTC Design Challenges

One of the challenges of transition metal UHTC carbides is their low ductility at room temperature. Below 1000°C UHTC carbides are brittle while above this temperature they can exhibit ductility and plastically deform [4,11]. In brittle behavior, the stress required to move dislocations is greater than the fracture stress, σ_y , and vice versa in ductile behavior. The ductile-to-brittle transition temperature, DBTT, is dependent on the carbide's inherent fracture strength which is based on stoichiometry and internal defects [4]. For instance, sub-stoichiometric phases will decrease the number of M-C, where M is the metal specie, bonds which may reduce the fracture strength [12] and internal defects (such as porosity) which affect the fracture strength [4]. Thus manipulating the fracture strength, by engineering and altering sub-stoichiometric phase development and internal defects will provide means to change mechanisms of deformation. Therefore, research in phase formation, microstructure, and internal defects are topics of relevance in improving fracture behavior in carbides.

Another material concern of UHTC carbides, is that they can oxidize at elevated temperatures. Thus, research on erosion resistance of UHTCs, mainly from oxidation, can lead to improved oxidation behavior materials for thermal design applications and thermal protection systems [13-16]. In general, the oxides that form may have different thermal expansion and conductivity properties which would lead to thermal shock, ablation, and erosion [2]. All of which is deferential to design performance. Research in UHTCs has presented multiple paths, systems with harmonious physical properties and/or the formation of protective barriers that achieve the same result: oxidation and erosion resistance [2].

1.2 Additives in UHTCs

The bulk of research on UHTCs has focused on how transition metals can improve the densification of ceramics with respect to processing techniques [13,17-24]. The density of the processed microstructure of these UHTCs has been related to mechanical properties such as Young's Modulus, fracture toughness, flexural strength, and oxidation resistance [13].

Initial issues for processing UHTCs were densification of the carbide, even after sintering and HIPing. Scholz recognized that small amounts of Fe strongly affected the sintering of refractory materials because of the formation of a liquid phase [17]. Other transition metals such as Mn, Co, and Ni had similar effects as Fe; they reduced the onset temperature for densifications for carbides [18]. Roeder and Klerk were able to hot press high-purity TaC powders with 1 wt% Mn or Ni additions [19]. It should be noted that Roeder and Klerk lowered the densification onset temperature, but the presence of a liquid phase resulted in exaggerated grain growth and entrapped porosity which prevented the ceramics from reaching full density [19]. Near full density was achieved by Fischer [20] for a TaC-HfC ceramic and by Ramqvist [21] for a TaC-NbC ceramic. Yohe and Ruoff obtained 93% density for TaC powder by removing the larger TaC particles [22]. Alternatively, Leipold and Becher used fine TaC powders and found that the composition affected the densification of TaC during hot pressing [23].

Oxide impurities have been observed on particle surfaces during the sintering of ceramics; TaC, NbC, TiB₂, SiC, B₄C, and ZrB₂ [18]. It was found that reactive additives such as C and B₄C were able to remove oxides in SiC, B₄C, and ZrB₂ in order to promote densification [18]. Research for low temperature oxidation behavior of Ta₂C with Al additions has found that at 600°C the Ta₂AlC system forms an oxide layer that prevents further oxidation. It was noted

that this system forms Ta_2O_5 and $TaAlO_4$ oxides which were uniform, porous, and highly cracked [25]. In general, it has been found that oxygen impurities in initial ceramic powders promote grain growth and inhibit densification.

1.3 Tantalum-Hafnium-Carbide System

1.3.1 The Tantalum-Carbon System

The B1 phase of γ -TaC has a melting temperature near 3900°C [26], Figure 1-1, and can exhibit plasticity at temperatures greater than 1500°C [11]. These attributes make TaC a candidate material for ultra-high temperature structural applications. When carbon is depleted from γ -TaC, the metastable rhombohedral ζ - Ta_4C_3 and/or trigonal Ta_2C phases can precipitate within the γ -TaC matrix, Figure 1-2. The Ta_2C phase begins to precipitate below 3500°C and has hexagonal metal layers separated by α -order (CdI antitype structure) or β -disordered ($L'3$ structure) carbon sublattices [27]. The Ta_2C phase has an allotropic phase transformation at 2000°C between the α -ordered and β -disordered phases. Both, ζ - Ta_4C_3 and Ta_2C β -phases, offer similar high melting points [27,28]. In general, it was found that the microstructure of tantalum carbides is dependent on carbon content as shown in Figure 1-3. The microstructure transitions from equiaxed to acicular and back to equiaxed morphology with decreasing carbon content [29] and various phase content.

It has been reported that variations of carbon in the tantalum-carbon system effect material properties such as micro hardness [30], electrical resistivity [30,31], thermodynamic properties [31,32], lattice parameters [33-35], and superconductivity [36]. Santoro found that a maximum in micro hardness, a minimum in tensile strength and a minimum in bend moduli and deflection, occurred in the tantalum-carbon system for compositions between $TaC_{0.8}$ and $TaC_{0.85}$ [37]. The ability to manipulate TaC's microstructure with secondary phases offers several

opportunities to tailor the thermo-mechanical properties via microstructure engineering. The mechanical behavior of the tantalum-carbon system could make it amenable to traditional metallurgical engineering techniques, such as solid solution strengthening. These solid solution strengthening additives could influence the microstructure formations through the processing of the carbide by altering phase transformation pathways as well as grain shape and size.

A major concern of tantalum carbides is its ready oxidation into Ta_2O_5 [9]. The common oxide phase for the tantalum-carbide system is Ta_2O_5 , Figure 1-4, which forms as triclinic, monoclinic, orthorhombic, tetragonal, and hexagonal dependent on temperature [38-42]. It has been shown that refractory ceramics at elevated temperatures are capable of forming low oxygen permeability interfaces which act as a protective oxygen barrier [2,13,14]. It is believed that a $(TaC)_{100-x}(HfC)_x$ system is capable of forming a protective oxygen barrier, an oxy-carbide interlayer, which could slow oxygen diffusion into the matrix. The tantalum-carbon system alone forms a porous oxide scale that has a low melting temperature, below $2000^\circ C$ [9], and fails due to non-dense oxide scale spalling [43]. Between $1400^\circ C$ and $1800^\circ C$ the hafnium-carbon system has shown an oxidation resistance behavior due to slower oxygen diffusion through a tetragonal HfO_2 oxy-carbide interlayer [44,45]. Thus, could additives be used to engineer the microstructure for improved mechanical responses as well as improved oxidation resistance?

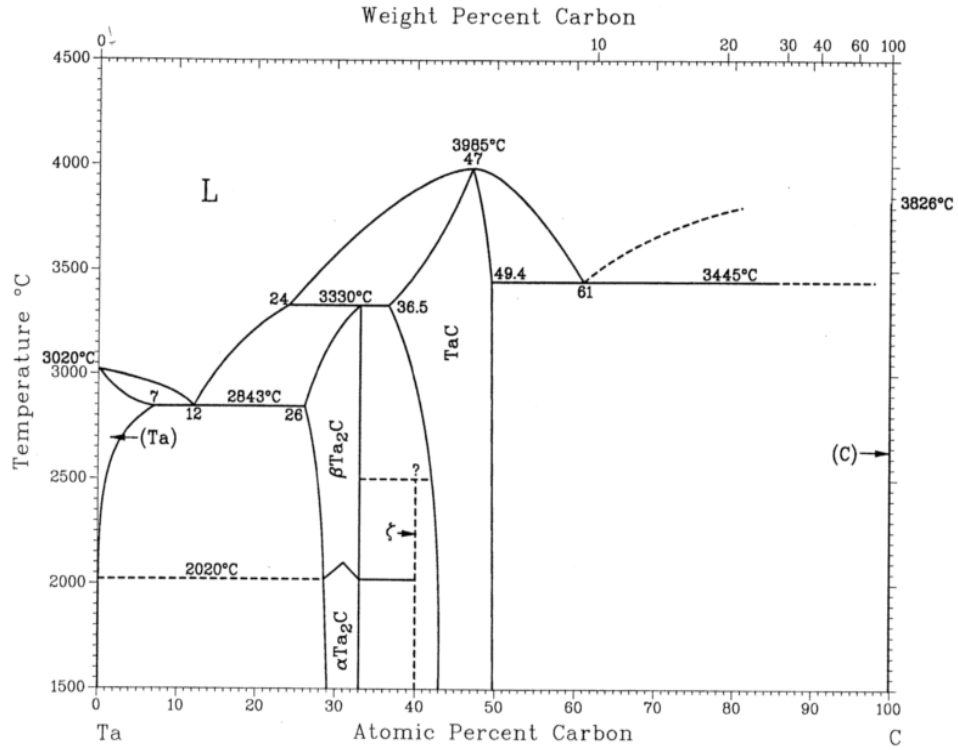


Figure 1-1 The tantalum-carbon binary phase diagram. [46]

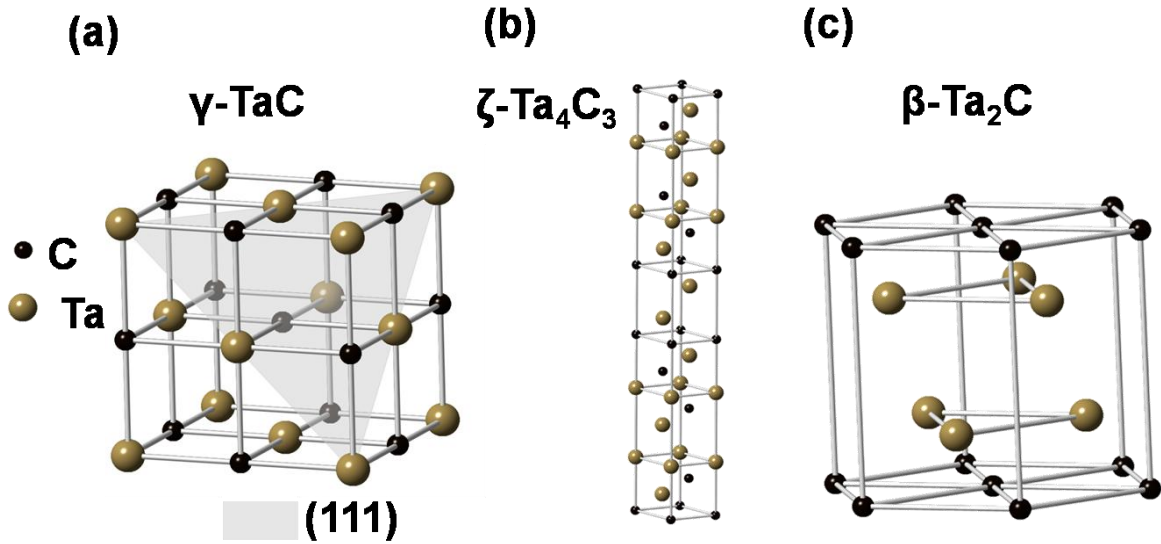


Figure 1-2 The (a) B1 rock-salt structure γ -TaC [47], the (b) rhombohedral ζ -Ta₄C₃ [48] and (c) β -Ta₂C [49] crystal structure. [29]

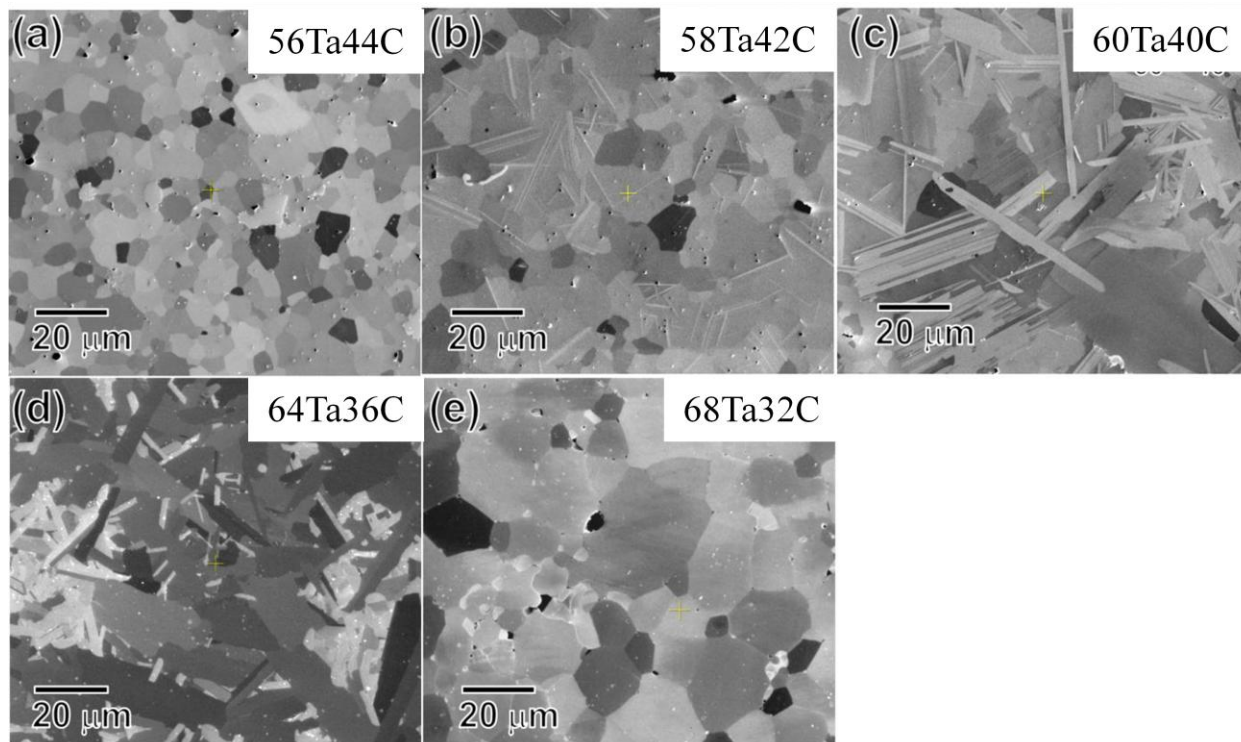


Figure 1-3 Morphology changes in tantalum carbide microstructures based on carbon content for (a) 56Ta44C, (b) 58Ta42C, (c) 60Ta40C, (d) 64Ta36C, and (e) 68Ta32C. [29]

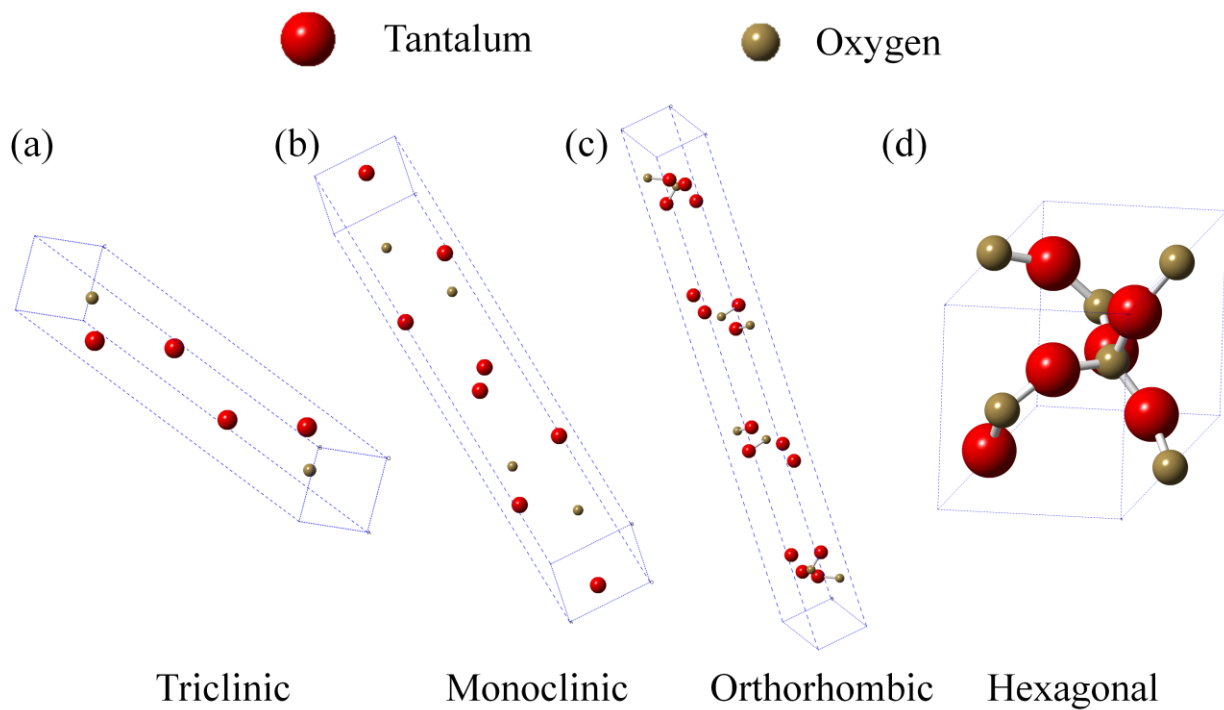


Figure 1-4 The crystallographic structures of Ta_2O_5 : Triclinic (a), Monoclinic (b), Orthorhombic (c), and Hexagonal (d). [38-41]

1.3.2 The Hafnium-Carbon System

Similar to γ -TaC, HfC is a B1 phase, Figure 1-5. When added to TaC, the hafnium can form a solid solution by occupying sites in the tantalum sub-lattice. Unlike the tantalum-carbon system, depletions in carbon does not precipitate out sub-stoichiometric phases, such as M_2C and M_4C_3 where again M is the metal specie, in binary Hf-C [50], Figure 1-6. Arguably, the majority of research on the hafnium-carbon system is associated with the processing of thin filmed HfC for electronic and magnetic applications [51,52]. Unlike TaC, the HfC does show improved oxidation resistance [44,45]. The common oxide phase for the hafnium-carbide system is HfO_2 , Figure 1-7, which forms as monoclinic, orthorhombic, and tetragonal dependent on temperature [53-55].

1.3.3 Mixing Tantalum-Hafnium-Carbon

It has been reported that the compositional mixture of TaC and HfC has the highest melting point near 4000°C [26,56,57]. The $(TaC)_{100-x}(HfC)_x$ system has the lowest thermal expansion coefficient [56]. In addition, it is believed that a $(TaC)_{100-x}(HfC)_x$ system is capable of forming a protective oxygen barrier, an oxy-carbide interlayer, which can reduce oxygen diffusion into the matrix [44] [45].

To date, there has been limited work in understanding how hafnium additions would change the phase and microstructure in $(TaC)_{100-x}(HfC)_x$ on tantalum oxidation behavior. In general, it is understood that among the UHTCs that borides are the most oxide resistant and the tantalum-carbide system is one of the least oxide resistant [58-60]. It has been found that the addition of hafnium to UHTC borides and carbides has shown improvements on the densification and mechanical properties of formed oxides [61]. The proceeding work will strive to contribute

towards that understanding. The work will focus on microstructure, grain size, porosity, phase formation, micro hardness, and oxidation behavior.

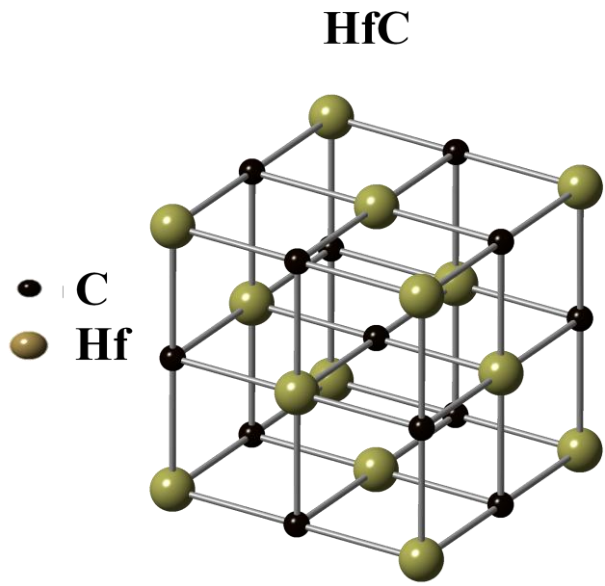


Figure 1-5 The B1 rock-salt structure HfC [62]

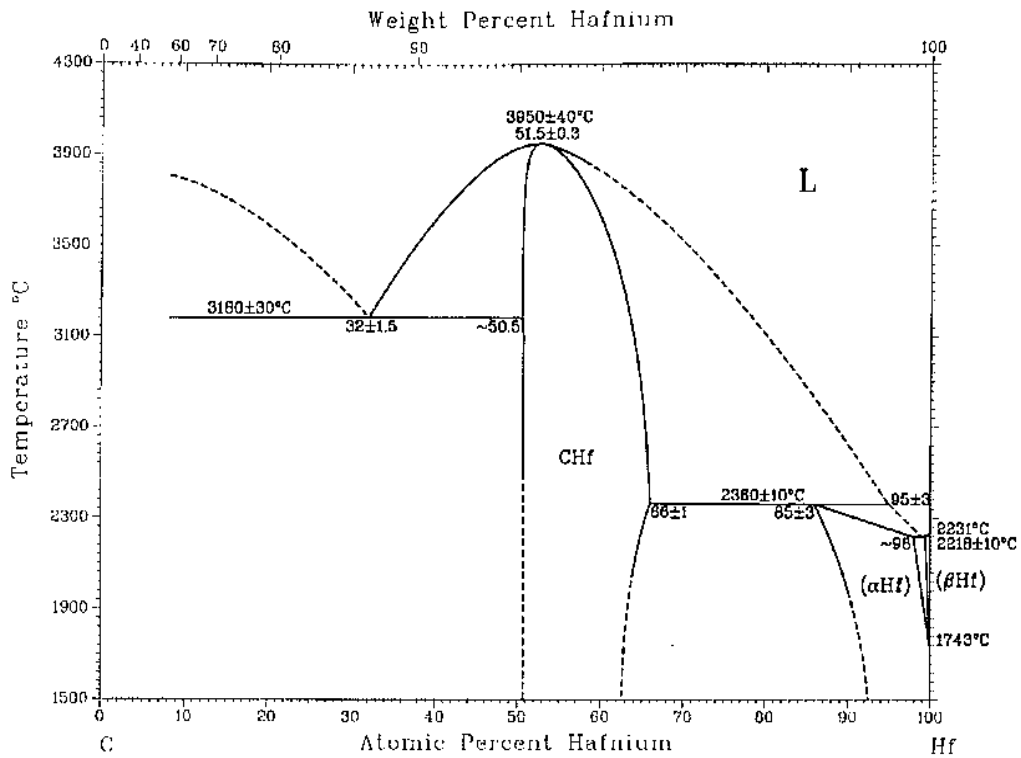


Figure 1-6 The hafnium-carbon binary phase diagram. [50]

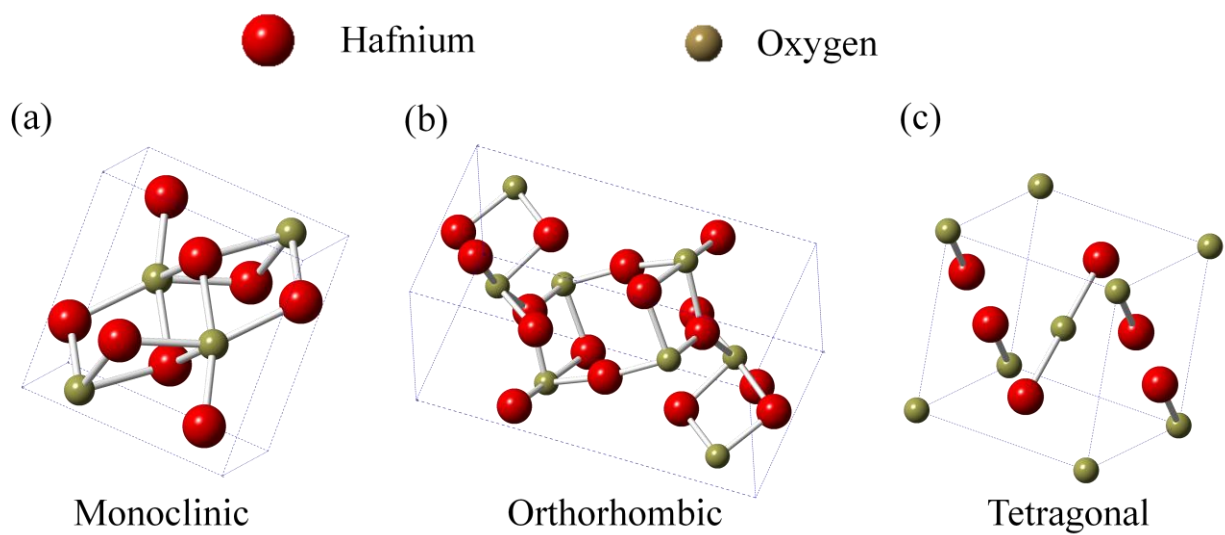


Figure 1-7 The crystallographic structures of HfO_2 : Monoclinic (a), Orthorhombic (b), and Tetragonal (c). [53-55]

1.4 UHTC Processing

The high melting temperatures of UHTCs requires specialized processes for both bulk and coating based fabricated parts. The ‘top-down’ process starts at a high temperature where upon the phases generally form by solidification. The ‘bottom-up’ heats the samples up below T_m and then returns to room temperature. Differences in heating and cooling rates along with different thermodynamic ‘top-down’ or ‘bottom-up’ processes will impact phase formation, microstructures, and porosity. Porosity has been found to affect the mechanical properties in the tantalum-carbon system [11]; however, general work on the formation of porosity in the tantalum-carbon and $(TaC)_{100-x}(HfC)_x$ systems is limited [63,64].

1.4.1 ‘Top-Down’ Processing

The ‘top-down’ processes used in this research are the vacuum plasma spray method (VPS) and the arc melt powder process (AMPP). For the VPS process, the mixed powders are fed into a plasma torch where the powders are melted and accelerated onto a graphite mandrel for rapid solidification. Similarly, the AMPP feeds powders in an electrical arc which melts them into a solidified mixture. The arc molten pellet is then crushed to form starting powders which can be sintered. Under both of these melting operations, carbon loss can and often does occur because of temperature-vapor pressure issues, reactions with processing gases, etc [65,66]. This will be described in more detail in the subsequent sections of this thesis.

1.4.2 ‘Bottom-Up’ Processing

The ‘bottom-up’ processes used in this research are sintering and hot-isostatic pressing (HIP) procedures for the VPS material, and spark plasma sintering (SPS) and HIPing procedures for the AMPP-SPS material. In general, HIPing is a process that involves solid-state diffusion of desired powder mixtures with slow heating and cooling rates. The procedure uses simultaneous

high pressures which allow significant plastic flow in the billet which yields near theoretical densities [67]. The simultaneous application of high pressures and slow heating rates eliminate micro porosity through creep and diffusion bonding [67]. Spark plasma sintering combines external pressure with an electric field simultaneously which enhances the densification of the powders [68]. The SPS process has shown greater densification than typical sintering techniques and occurs at lower temperatures for shorter times [69,70]. The SPS process produces a DC pulse current which creates a high-energy plasma between the gaps of the powders and an electrical field diffusion effect [71]. Prior research involving SPS processing have reported the use of low pressures, 30 MPa, and temperatures in the range of 1900-2400°C. Densification for sintering at 1900°C for 5 min lead to 68% density of TaC powders while 2400°C lead to 97% density. Grain size was reported as being unaffected by sintering temperature [69,70].

Chapter 2 Experimental

2.1 Vacuum Plasma Spray Processing

Four specimens of $(\text{TaC})_{100-x}(\text{HfC})_x$, where X is based on the starting blended powder compositions of 0.3, 3.0, 16.5, and 19.8 at.%, were fabricated by a ‘top-down’ vacuum plasma spraying (VPS). The feedstock powders were mechanically mixed from monocarbide TaC and HfC powders to the appropriate atomic fraction. The VPS processing chamber was evacuated to 100 mTorr using mechanical pumps whereupon it was backfilled with argon to a pressure of 200 Torr. A volume mixture of 70:1 Ar:H₂ served as the processing gas for the feedstock powder through the VPS tungsten cathode plasma gun. From the plasma gun, the molten feedstock powder was sprayed onto a rotating graphite mandrel. Post-VPS fabrication, the graphite mandrel was mechanically ground away from the $(\text{TaC})_{100-x}(\text{HfC})_x$. The carbide material was then sintered near $\frac{1}{2} T_m$, where T_m is the melting point, in a graphite furnace under vacuum to reduce porosity inherent in the VPS fabrication method [63]. Post-sintering, these materials were approximately 95±2% dense. To further reduce porosity, the post-sintered specimens were HIPed to reach a density near 98±2%. The reported densities were measured using a displacement fluid technique (Archimedes principle) with single phase $(\text{TaC})_{100-x}(\text{HfC})_x$ as the base-line metric. As will be seen below, some of these specimens precipitated out other phases which would alter the absolute density values reported for these specimens therefore the densities given are approximate. The VPS specimens were supplied to the research project through collaboration with Dr. Daniel Butts, Plasma Processes LLC. (Huntsville, AL).

2.2 Arc-Melt Powder Processing

Four specimens of $(\text{TaC})_{100-x}(\text{HfC})_x$, where X is based on the starting blended powder compositions of 5.8, 10.7, 17.6, and 25.0 at.%, were fabricated by an AMPP. These AMPP powders then underwent HIPing and spark plasma sintering (SPS). A general SPS process run is carried out in argon atmosphere at 1850°C with the heating rate of 200°Cmin⁻¹ to the maximum temperature with a hold time of 10 min. The pressure applied ranges from 100 MPa to 365 MPa [69,70]. The AMPP-SPS specimens were supplied to the research project through collaboration with Dr. Larry Matson, Air Force Research Lab (Wright-Patterson Air Force Base, OH), and Dr. Heedong Lee, United Energy System, Inc. (Dayton, OH).

2.3 General Specimen Preparation

All specimens were mounted in a conductive material and mechanically polished using 3 μm diamond paste with a further polish for 24 hours in aqueous 0.05 μm silica slurry using a Vibromet. This latter polishing step was found to be critical in surface preparation to reveal and characterize the microstructure.

2.4 Specimen Characterization

The following instruments and techniques were used to characterize the processed specimens. Detailed procedures are given in the proceeding sections. The results and calculations incorporated with them may be found in the following chapter and appendix.

2.4.1 FEI Quanta 3D FIB

Microstructure characterization and imaging was performed using a FEI Quanta 3D dual scanning electron (SEM) – focus ion beam (FIB) microscope. The images were collected in either an ion contrast imaging condition at 30 keV or secondary electron (SE) or backscattered

electron (BSE) conditions between 20-30 keV. The specimen grain size was quantified using Electron Backscattered Diffraction (EBSD) patterns taken on an EDAX-TSL Hikari camera platform attached to the Quanta 3D. The specimens were tilted 70° towards the EDAX-TSL detector and scanned at 100 frames per second with the electron beam at 30 keV and 5 nA. The TSL software calculated grain size analysis and statistics. The porosity fraction was based on the Delesse Principle which compares the surface area fraction of the total pore count divided by the total surface area of the image [72].

2.4.2 Bruker D8 GADDS

The phase and volume fraction analysis was done by X-ray diffraction (XRD) using a Bruker D8 Discovery General Area Diffraction Detector System (GADDS) using Cu-K α radiation at 45 keV and 40 mA as the source. The collected peaks were compared with the lattice structure data in the ICDD cards of references [38-49,53-55,73-75]. Prior to XRD analysis, the specimens were crushed and ground using a mortar and pedestal which ensured a random texture and sufficiently large sampling volume from the powder particulates. The volume fraction of the phases was estimated by taking the experimental peak which corresponded to the most intense ICDD calculated peak and dividing its integrated intensity by the sum of all the integrated intensities of the phases' most intense peaks in the spectra.

2.4.3 FEI F20 Tecnai

Bright and dark field imaging on the FEI F20 Tecnai transmission electron microscope (TEM) operated at 200 keV was used for microstructure analysis. The High Angle Annular Dark Field (HAADF) detector was used for Z-contrast imaging in the scanning transmission electron microscope (STEM) mode. The Z-contrast imaging observed is chemically dependent with

higher atomic number elements being brighter since the HAADF collects scattered electrons that are insensitive to crystallographic dependent scattering [76]. TEM specimens were prepared using a FIB milling technique which allowed for site specific extraction and thinning [77,78].

2.5 Knoop Micro-Indentation Hardness Measurements

Specimens underwent Knoop micro-indentation testing, the preferred method for ceramics, at room temperature for hardness and crack propagation behavior [79]. The Knoop hardness indentation is ideal for ceramics because of its elongated indent generation and low depth profile. The bulk specimens were tested before and after oxidation treatments at loads of 500g, 200g, and 50g on a Buehler 1600 Hardness Tester with a K-409 tip, Figure 2-1. The relative length of indentations provided semi-quantification of the relative fracture toughness, i.e. shorter indents is indicative of higher fracture toughness. Fracture toughness in the bulk of the carbide and the oxide scale were performed. After Knoop indentation, some specimens were selected for FIB milling in order to make site specific TEM specimens for further analysis.

2.6 Oxidation Heat Treatments

Partitions were cut from the specimens and underwent oxidation heat treatments. The mass of the pieces were measured before and after oxidation treatment for mass change analysis. These specimens were placed in alumina boats and heated in a Paragon PMT10 box furnace at 1680W, 120V, and 14A under atmospheric conditions. The oxidation treatment in the box furnace consisted of a 300°C/hr heat ramp to 1000°C where it was held for 30 min and cooled off to 200°C for 2 hrs for consistency before removal. The general heating rates for the treatment are summarized in Figure 2-2.

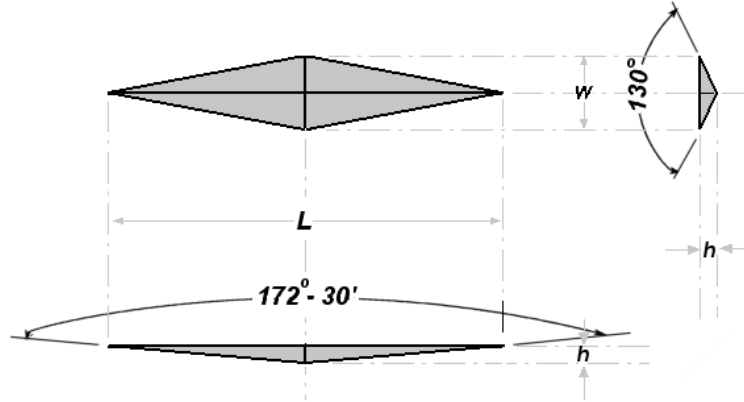


Figure 2-1 Knoop indentation schematic drawings. [79]

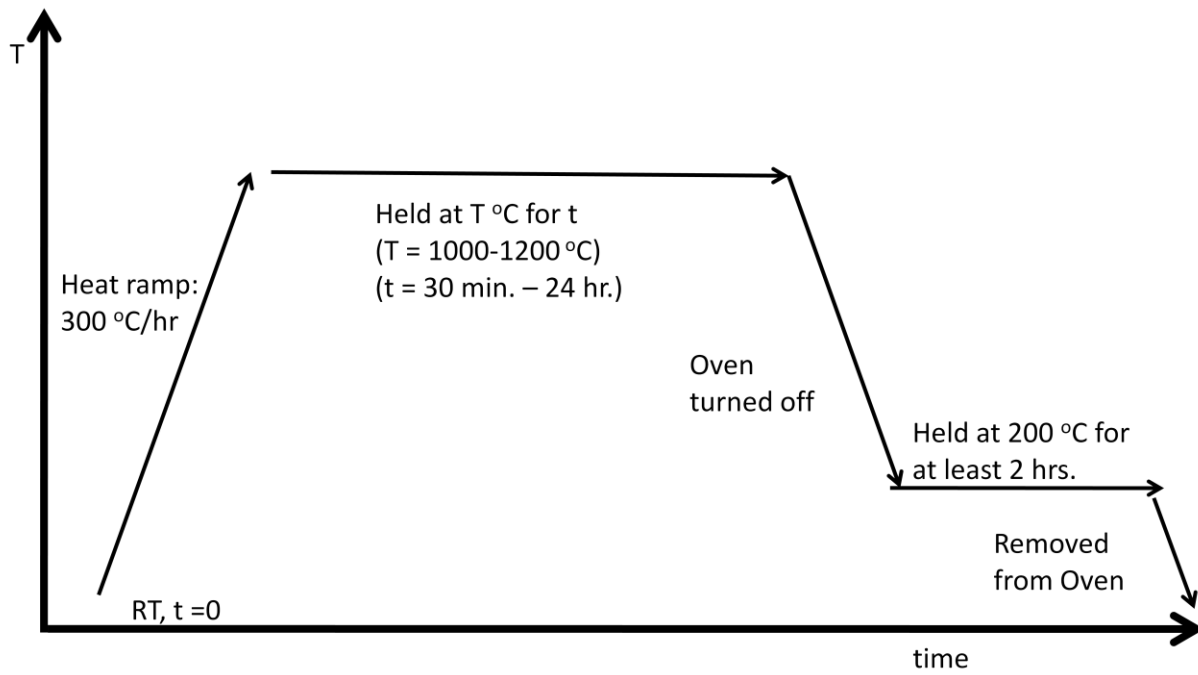


Figure 2-2 Schematic drawing of heat treatments for oxidation analysis.

Chapter 3 Microstructure and Phase Formation

3.1 VPS and AMPP-SPS Processed $Ta_{1-x}Hf_xC$ Microstructure and Phase Results

The following details the findings from the microscopy characterization of the $(TaC)_{100-x}(HfC)_x$ specimens, where X is between 0.3 and 25.0 at.%, for phase identification, microstructure grain size, and porosity. The first group of specimens, the VPS processed specimens where X is 0.3, 3.0, 16.5, and 19.8 at.%, has summarized results in Table 3-1. The second group of specimens before oxidation, the AMPP-SPS processed specimens, where X is 5.8, 10.7, 17.6, and 25.0 at.%, has summarized results in Table 3-2.

Table 3-1 Initial volume phase %, porosity %, mean grain diameter, and estimated carbon loss during VPS processing of tantalum-hafnium carbides with respect to at.% HfC.

Nominal Composition $(TaC)_{100-x}(HfC)_x$	Phases (%)		Porosity (%)	Mean Grain Diameter (μm)	Estimated Carbon Loss (at.%)
0.3 at.%	Ta(Hf)C [111]	47	1.6	14.9 ± 4.0	13.4
	Ta ₂ C [1011]	9			
	Ta ₄ C ₃ [107]	44			
3.0 at.%	Ta(Hf)C [111]	67	1.2	10.5 ± 1.5	13.2
	Ta ₂ C [1011]	9			
	Ta ₄ C ₃ [107]	24			
16.5 at.%	Ta(Hf)C [111]	80	2.1	1.8 ± 1.0	14.6
	Ta ₂ C [1011]	20			
	Ta ₄ C ₃ [107]	0			
19.8 at.%	Ta(Hf)C [111]	87	2.5	2.8 ± 0.6	13.2
	Ta ₂ C [1011]	11			
	Ta ₄ C ₃ [107]	2			

Table 3-2 Initial volume phase %, porosity %, mean grain diameter, and estimated carbon loss during AMPP-SPS processing of tantalum-hafnium carbides with respect to at.% HfC.

Nominal Composition (TaC) _{100-x} (HfC) _x	Phases (%)		Porosity (%)	Mean Grain Diameter (μm)	Estimated Carbon Loss (at.%)
5.8 at.%	Ta(Hf)C [111]	58	1.4	7.1 ± 0.8	17.7
	Ta ₂ C [1011]	42			
	Ta ₄ C ₃ [107]	0			
10.7 at.%	Ta(Hf)C [111]	48	2.7	4.6 ± 0.3	19.1
	Ta ₂ C [1011]	52			
	Ta ₄ C ₃ [107]	0			
17.6 at.%	Ta(Hf)C [111]	55	5.1	2.6 ± 0.1	18.1
	Ta ₂ C [1011]	45			
	Ta ₄ C ₃ [107]	0			
25.0 at.%	Ta(Hf)C [111]	45	4.7	1.6 ± 0.1	19.5
	Ta ₂ C [1011]	55			
	Ta ₄ C ₃ [107]	0			

3.1.1 Microstructure and Grain Size

An increase in HfC content resulted in the reduction of the equiaxed grain size, as shown in Figure 3-1 and Figure 3-2. The calculated grain sizes were plotted with respect to initial HfC content, Figure 3-3 and Figure 3-4. The secondary phase laths of Ta₂C and/or Ta₄C₃, commonly observed in TaC grains [48,63,80,81], were too narrow to be reliably indexed in the EBSD scans shown and have not been included. However, they were easily observed in the ion contrast images and were encased within the grains, as reported in references [48,63,80,81] and seen in Figure 3-5 and Figure 3-6.

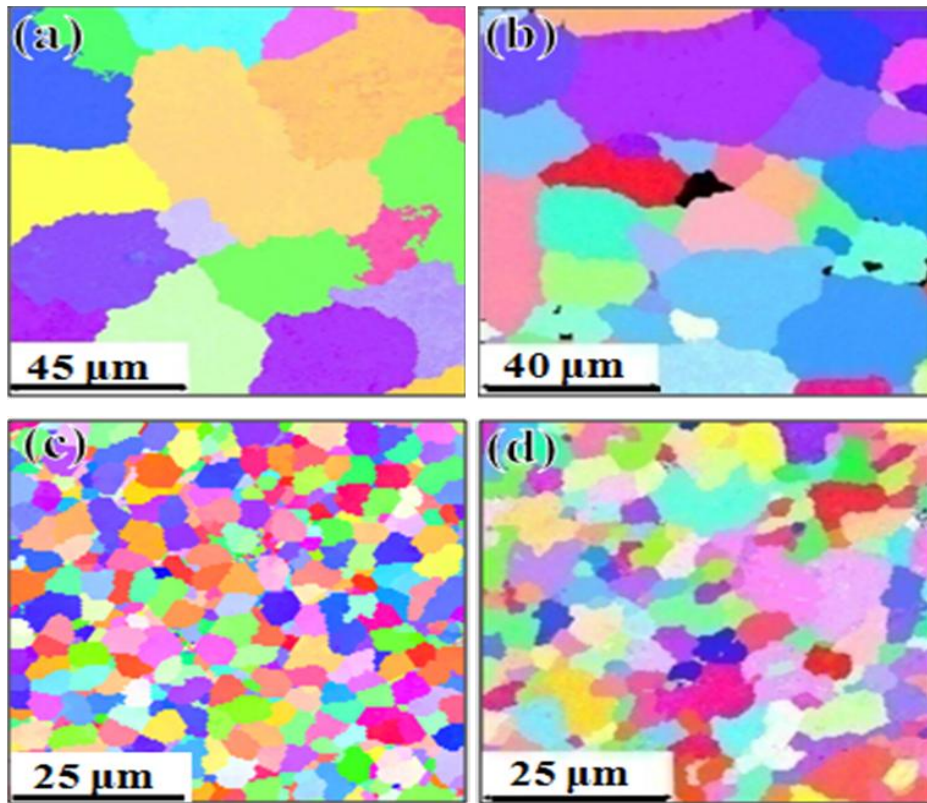


Figure 3-1 Representative EBSD images of (a) 0.3 at.% HfC, (b) 3.0 at.% HfC, (c) 16.5, and (d) 19.8 at.% HfC VPS processed specimens. The black regions represent pores.

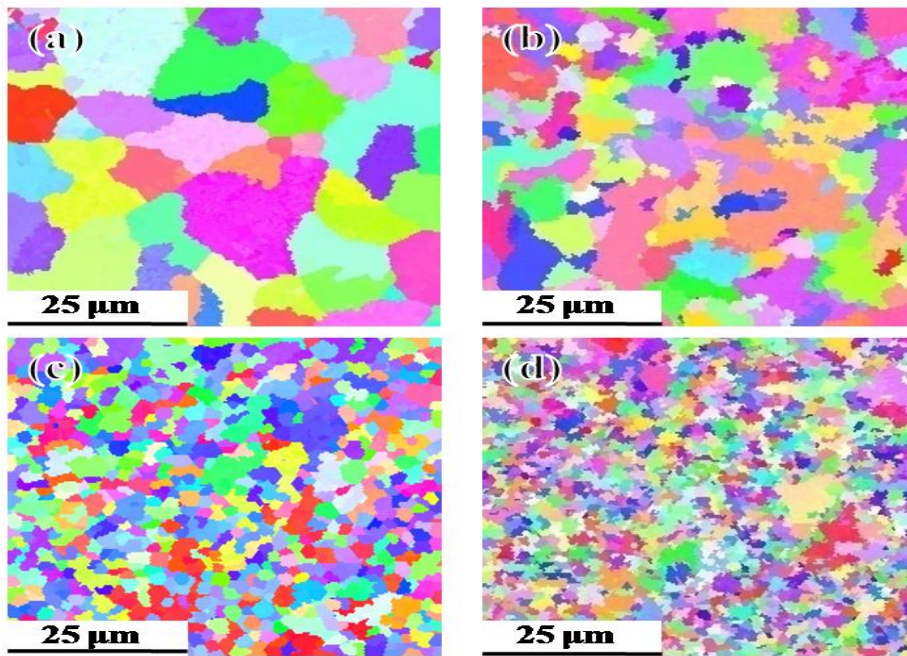


Figure 3-2 Representative EBSD images of (a) 5.7 at.% HfC, (b) 10.7 at.% HfC, (c) 17.6 at.% HfC, and (d) 25.0 at.% HfC AMPP-SPS processed specimens. The black regions represent pores.

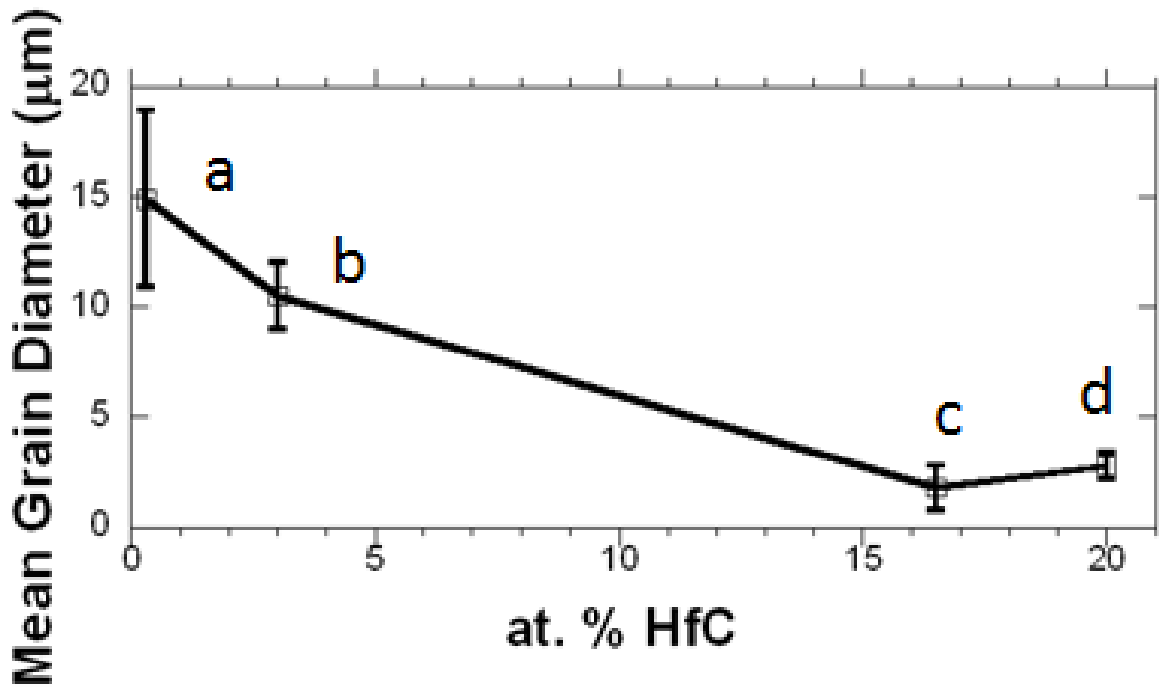


Figure 3-3 Mean grain diameter plotted against at.% HfC taken from Figure 3-1(a-d) for VPS processed specimens.

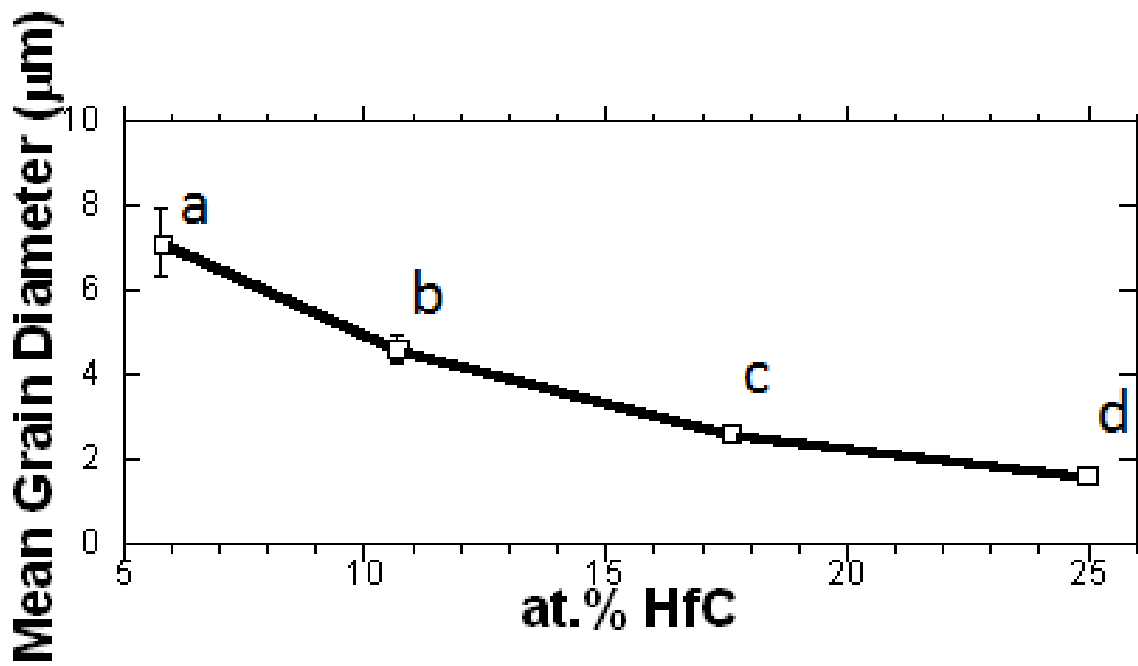


Figure 3-4 Mean grain diameter plotted against at.% HfC taken from images Figure 3-2(a-d) for AMPP-SPS processed specimens.

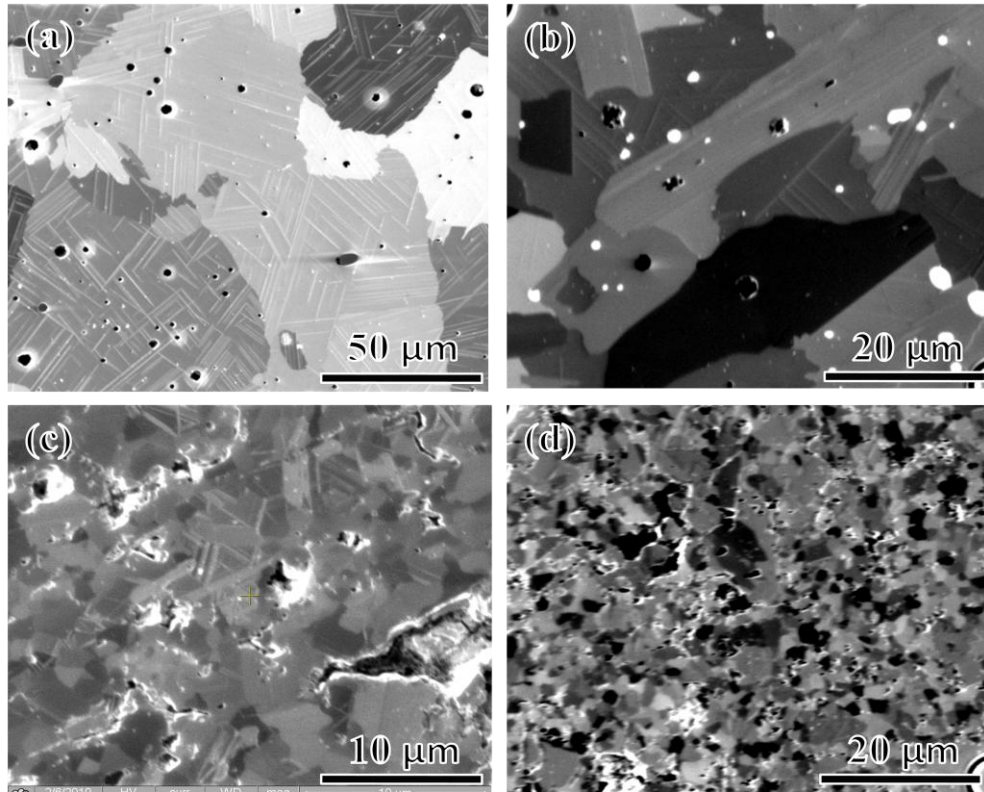


Figure 3-5 SEM-FIB ion contrast images of the (a) 0.3, (b) 3.0, (c) 16.5, and (d) 19.8 at.% VPS processed microstructures.

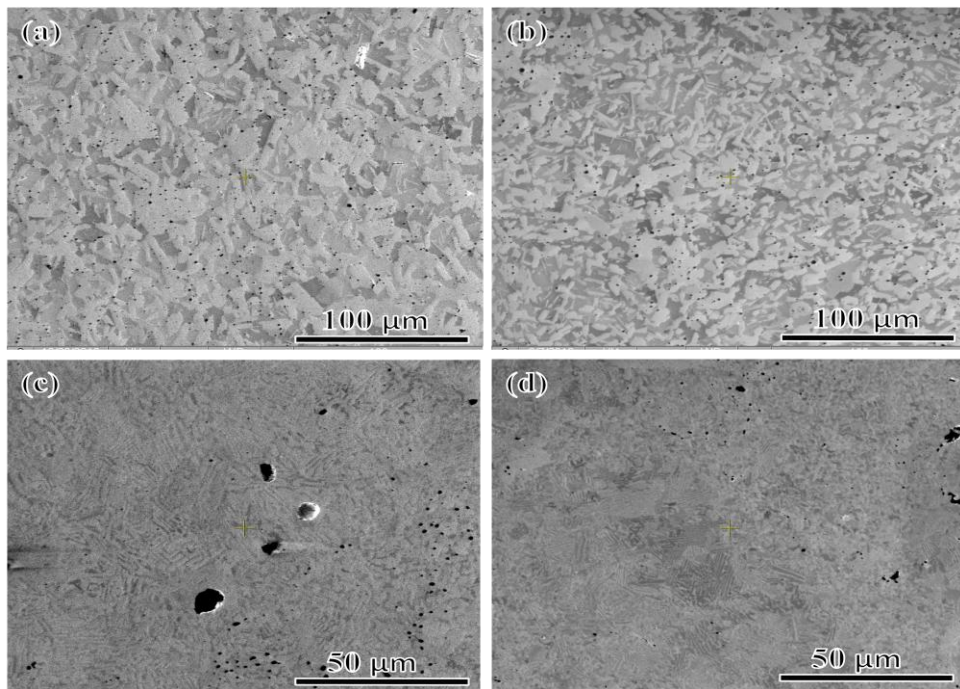


Figure 3-6 SEM-FIB ion contrast images of bulk regions for the (a) 5.8, (b) 10.7, (c) 17.6, (d) and 25.0 at.% AMPP-SPS processed specimens.

The TEM was used to locate and identify the secondary sub-stoichiometric phases found in the XRD scans. Figure 3-7 shows TEM images from the 19.8 at.% specimen with the dark field patterns for each image. Three separate orientations of the same viewing area were used to identify the lathes. These viewing orientations were $\langle 011 \rangle$, $\langle 112 \rangle$, and $\langle 011 \rangle$. These different orientations created “visible” and “invisible” viewing perspectives of the laths. The “visible” conditions are marked by black arrows and “invisible” by white arrows for the same lath. The laths shown in the last two orientations, $\langle 112 \rangle$ and $\langle 011 \rangle$ but not the first, are so thin that their edges do not generate sufficient diffraction contrast making them appear “invisible”. Thus, one should be careful in image interpretation of the microstructure and perform a tilt series to ensure all features in the microstructure are accounted for.

3.1.2 Porosity

Besides the smaller grain sizes, the porosity also increased with an increased HfC content, Table 3-1 and Table 3-2. The greater HfC content specimens, 16.5 and 19.8 at.% HfC for the VPS process and 17.6 and 25.0 at.% HfC for the AMPP process, have nearly double the amount of porosity as compared to the lower HfC content species. The majority of the pores were observed to be between the grains rather than within the grains for these specimens. An example porosity calculation can be found in Appendix 7-4.

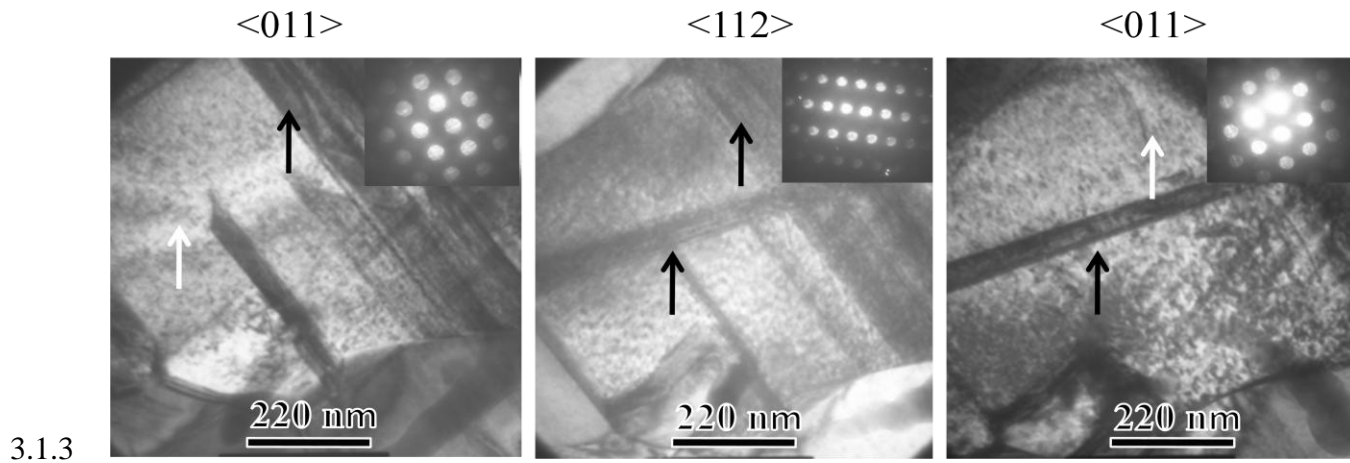


Figure 3-7 Dark field images from TEM for the 19.8 at.% specimen for $\langle 011 \rangle$, $\langle 112 \rangle$, and $\langle 011 \rangle$ orientations. The white arrows indicate invisible conditions while the black arrows indicate visible conditions.

3.1.4 Phase Characterization

The XRD spectra for each specimen are shown in Figure 3-8 and Figure 3-9 respectively for the VPS and AMPP-SPS processed specimens. The XRD scans for these specimens indicated that the AMPP-SPS compositions suppressed the Ta_4C_3 phase formation whereas the VPS compositions formed TaC, Ta_2C , and Ta_4C_3 . The VPS spectra confirm the presence of TaC, Ta_2C , and Ta_4C_3 with their corresponding lattice parameters plotted in Figure 3-10. This is in agreement with the TEM observations of secondary phase formation, Figure 3-7. A sample indexed spectra can be seen in Appendix 7-1. The TaC's lattice parameter increased with HfC content, Appendix 7-2, as would be expected since the larger hafnium atoms substitute within the tantalum sub-lattice. The Ta_2C 's hexagonal and Ta_4C_3 's rhombedral lattice parameters' a- and c- did not show any significant change. This result indicates that hafnium does not appear to substitute for tantalum in these sub-stoichiometric tantalum carbide phases. This too would be expected since these phases, M_2C and M_4C_3 , do not exist on the binary Hf-C phase diagram [46,50]. An example calculation of the phase volume % can be found in Appendix 7-3.

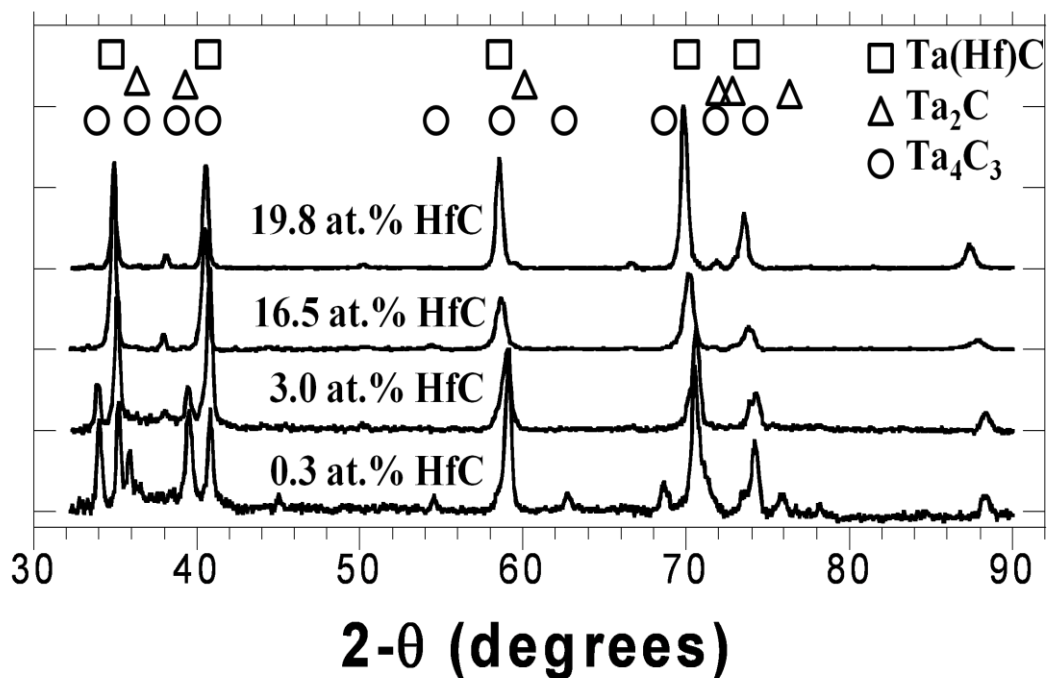


Figure 3-8 XRD results from the 0.3, 3.0, 16.5 and 19.8 at.% HfC VPS processed specimens. Each spectra revealed the phases TaC , Ta_2C , Ta_4C_3 at various diffracted intensities.

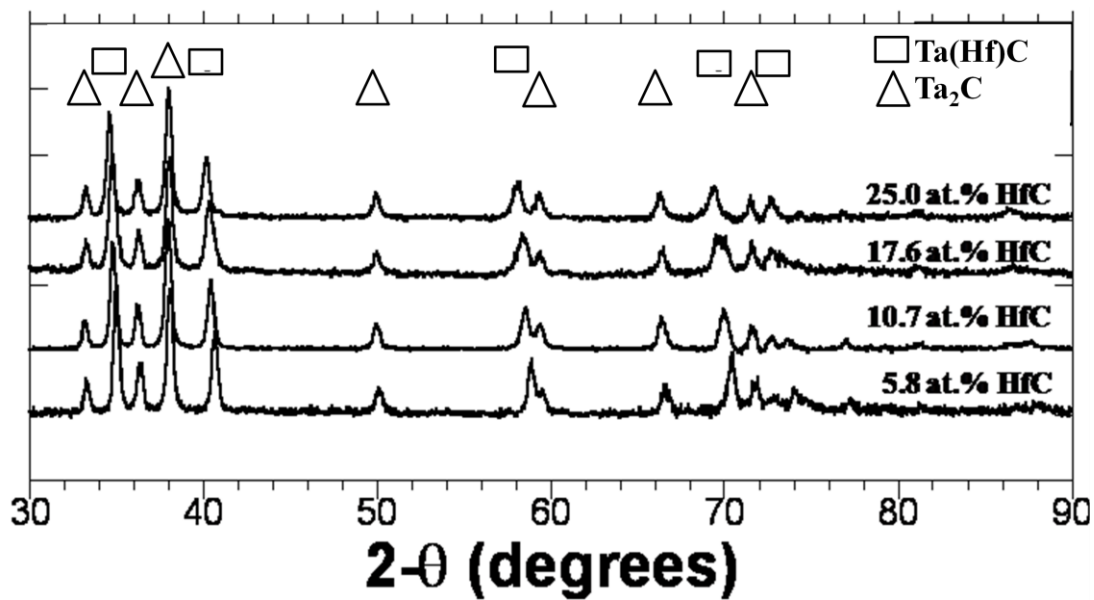


Figure 3-9 XRD results from the 5.8, 10.7, 17.6 and 25.0 at.% HfC non-oxidized AMPP-SPS specimens. Each spectra revealed the phases TaC and Ta_2C at various diffracted intensities.

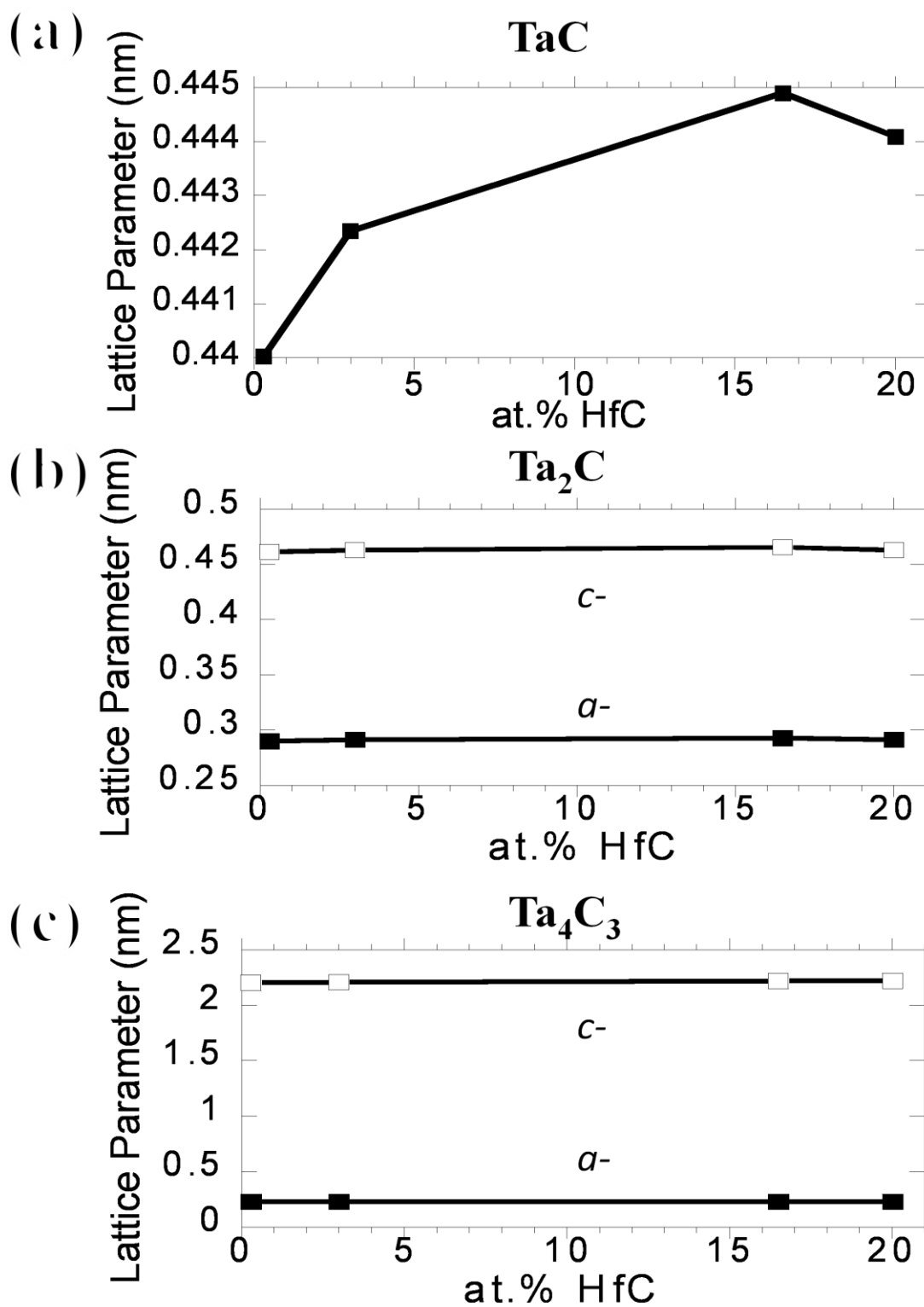


Figure 3-10 Lattice parameters with respect to at.% HfC for the VPS specimens (a) TaC cubic lattice parameter a -, (b) Ta₂C hexagonal lattice parameter a - and c -, and (c) Ta₄C₃ rhombohedral lattice parameter a - and c -.

3.2 VPS and AMPP-SPS $(\text{TaC})_{100-x}(\text{HfC})_x$ Microstructure and Phase Discussion

3.2.1 Grain Size and Porosity Analysis

Finer grain sizes are observed in higher at.% HfC specimens, Table 3-1 and Table 3-2, for the respective processes. Recall that VPS and AMPP-SPS processes involve a solidification-based step in either the initial as-sprayed grain size or starting powder mixtures. Morris [29] showed that the initial VPS grain size or powder size in HIP processing trended well with final grain size in post process homogenization treatments. Additionally, the processes initiated with monocarbide TaC and HfC powders but the final microstructures contained Ta(Hf)C, Ta₂C and/or Ta₄C₃ phases, indicating that some amount of carbon loss occurred. In general, the ternary phase diagrams, Figure 3-11, show that carbon loss occurs; the system is driven into a sub-stoichiometric and liquid phase field. This change in equilibrium phase content will be used to rationalize the refinement of grain sizes in these materials.

As HfC is added to TaC with the loss of carbon, the melting temperature will be suppressed [82]; this is seen in the phase diagrams of Figure 3-11. The subsequent solid phase precipitation will be at lower temperatures. Consequently, grains will have relatively lower mobility (growth) because of the reduced temperature as compared to compositions that precipitated at elevated temperatures. In addition, these compositions will be further under-cooled, and at a lower temperature, where the thermodynamic nucleation driving force will be high. This will result in numerous nucleation events resulting in a finer grain size.

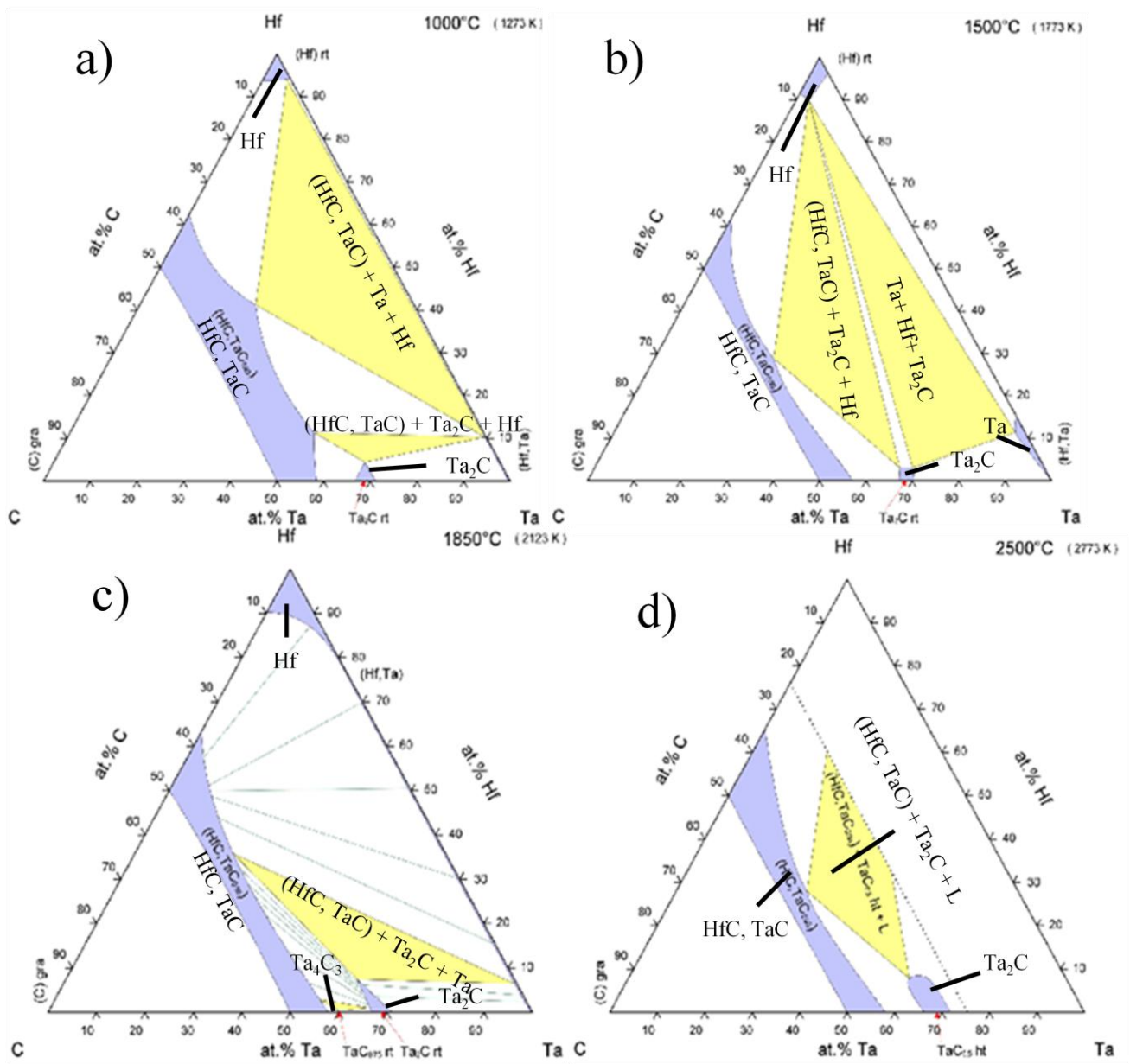


Figure 3-11 Ternary phase diagram for tantalum-hafnium-carbon at a) 1000°C, b) 1500°C, c) 1850°C, and d) 2500°C. [82-85]

To support this statement, an interface tracking model was constructed, in collaboration with Dr. Billie Wang, that showed the influence of the changing melting temperature on the microstructure during a continuous cool. Though the model is generic, the change in melting temperature reflects the Ta-Hf-C system's change in a liquid phase field. The model is based upon the four following assumptions: (A) Adding HfC to TaC and carbon loss decreases the melting temperature. (B) The mobility, M , has an Arrhenius relationship;

$$M = Ae^{\frac{-B}{T}} \quad (1)$$

where in equation (1) T is temperature, and A and B are generic parameters [86]. (C) The driving force for transformation nucleation, N , has an Arrhenius behavior proportional to the under-cooling squared and mobility;

$$N = Ce^{\frac{-D}{(T_m-T)^2}} \quad (2)$$

where in equation (2) T is temperature, T_m is the melting temperature, and C and D are generic parameters [86]. And (D) any transformed grain does not coarsen. The sequential images of the nuclei forming and growing are plotted in Figure 3-12. Figure 3-12(a) shows a decrease in grain size with respect to decreasing T_m , 4000 to 1500 arbitrary units (a.u.), for a hypothetical situation where $A = 148$, $B = 10,000$, $C = 0.1$ and $D = 10,000$ a.u. Figure 3-12(b) demonstrates the grain formation for $T_m = 3000$ a.u. with respect to time. The model does not predict the grain morphology but does estimate an average grain size. With a decrease in the melting temperature, this simple model does predict a greater concentration of grains, which are on average smaller. This is consistent with our results that higher HfC content specimens formed smaller grains.

The experimental results also showed an increase in porosity with HfC content. Porosity can form because of the volume change associated with the liquid to solid phase transformation. These pores can form between the grains as the solid phase contracts from each other. The

increase in the number of grains with HfC content yielded an increase in the amount of interfaces which would contract from each other and lead to a greater percentage of porosity as observed and tabulated in Table 3-1 and Table 3-2.

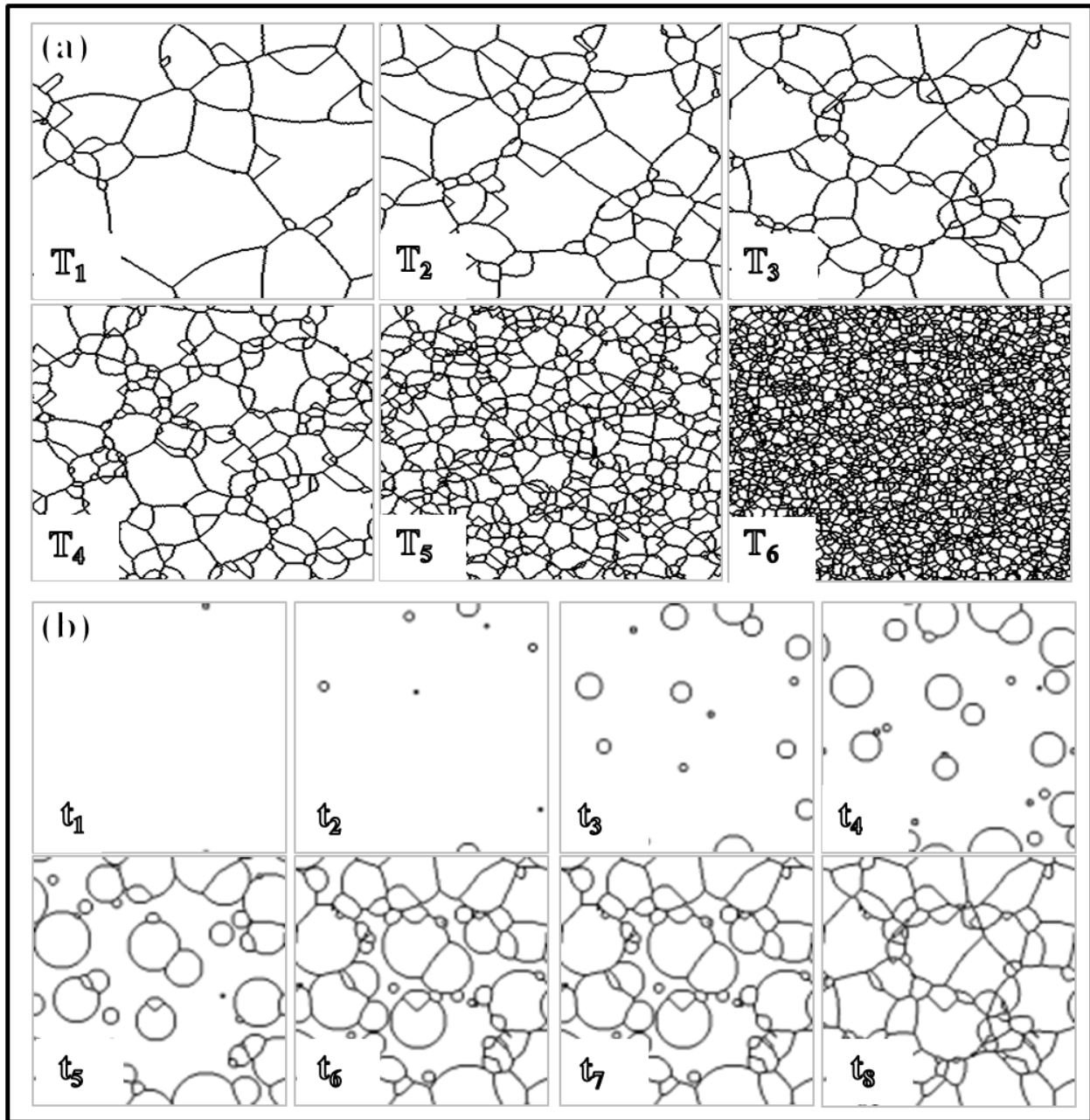


Figure 3-12 Interface tracking model results (a) microstructure grain size as T_m decreases from 4000 to 1500°C where $T_1 > T_2 > T_3 > T_4 > T_5 > T_6$ in the images and T represents temperature (b) Time evolution for T_m 3000°C where $t_1 < t_2 < t_3 < t_4 < t_5 < t_6 < t_7 < t_8$ in the images and t represents time.

3.2.2 Phase Formation

As already addressed, the processes have shown inherent carbon loss via XRD scans of tantalum rich carbide phases. The volume fraction of phases was also shown to be strongly dependent on HfC content. When both groups of processed specimens are collectively analyzed, Table 3-1 and Table 3-2, it is revealed that lower at.% HfC specimens, 0.3 and 3.0, have larger volume fractions of Ta_4C_3 . Though the ‘top-down’ processes are considered non-equilibrium, the phase formations can be explained by thermodynamic pathways based on chemical and compositional components. The phase diagrams [82,83], elemental vapor pressures [87], and diffusivity [88,89] serve as useful guides for thermodynamic pathways for phase stability.

The thermodynamic chemical explanation assumes carbon loss during the processing of the specimens. This has been experimentally confirmed by the precipitation of sub-stoichiometric tantalum carbide phases. Possible mechanisms for carbon loss during the processing include the formation of hydrocarbons [65] between the carbide powder and the plasma processing gas [66], as well as the higher carbon vapor pressure as compared to the tantalum species [87]. The continual loss of carbon is represented by the dashed and larger dotted lines in Figure 3-13(a) and (b). This line fixes the ratio of Ta-to-Hf content while changing the carbon content. As seen in Figure 3-13(b), the 0.3 and 3.0 at.% HfC specimens specifically enter the TaC and Ta_4C_3 two-phase region with carbon loss (dotted line). As the HfC content is increased from 3.0 at.% towards 19.8 and 25.0 at.% HfC, the stable solid phase field regions become TaC and Ta_2C . This explains the reduction (and absence) of Ta_4C_3 in the higher HfC content specimens, it does not feasibly form for specimens with HfC content greater than 4 at.% HfC. In general the VPS processed specimens, Table 3-1, showed an increase in volume fraction of TaC as HfC content increased while the AMPP-SPS processed specimens, Table 3-2 did not

show this similar trend. This difference will be addressed by considering the equilibrium tie lines that join the two phase fields.

During solidification, the VPS processed 19.8 at.% HfC specimen would be in the liquid phase field longer than the lower HfC containing specimens, therefore it would be expected to form more sub-stoichiometric phases, Figure 3-13(a), because of increased carbon loss.

However, this specimen has the lowest volume fraction of sub-stoichiometric tantalum-rich carbide phases, Table 3-1. In order to reconcile these two observations, the influence of hafnium content during solidification is considered. It is noted in Figure 3-13(b), as the hafnium content is increased, the length of the tie lines between the two stable phase regions increases. This indicates that for an equivalent amount of carbon loss, as hafnium content is increased, a greater volume fraction of the Ta(Hf)C B1 phase will form.

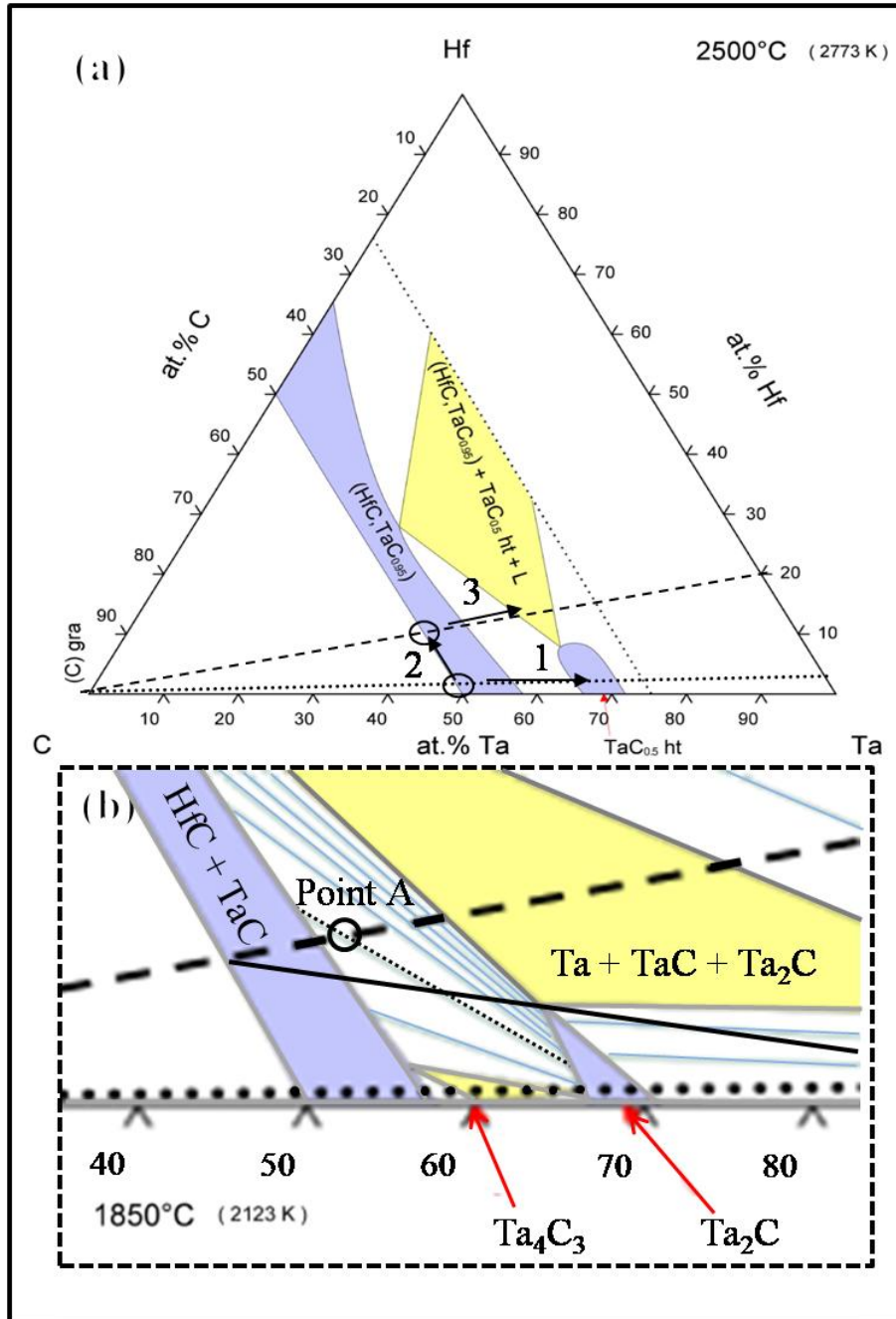


Figure 3-13 Ternary phase diagram of Ta-Hf-C at (a) 2500°C [83] with dashed lines indicating a continual carbon loss for 3.0 at.% HfC and 19.8 at.% HfC. Arrow 1 shows carbon loss for 3.0 at.% HfC. Arrow 2 points in the direction of phase field stability with an increase from 3.0 at.% to 19.8 at.% HfC. Arrow 3 shows carbon loss for 19.8 at.% HfC. (b) The region of interest on the 1850°C [82] phase diagram is magnified; the carbon loss for 3.0 at.% (dotted line) and 19.8 at.% HfC (dashed line) are marked. The fine dotted line represents the tie-line between the TaC+HfC phase field and Ta₂C for Point A, located approximately at 13 at.% carbon loss. The solid line represents equal loss of carbon and hafnium for the 19.8 at.% HfC specimen.

The carbon loss for the specimens was estimated by analyzing the equilibrium concentrations of the phases at 1850°C [82], Figure 3-13(b), with respect to the volume fractions of phases in Table 3-1 and Table 3-2. The approximate carbon loss was calculated by comparing the volume fractions of the phases with respect to adjusted tie lines on the phase diagram, Appendix 7-5. These calculations show near equivalent carbon loss of approximately 13-14 at.% for the VPS specimens, Table 3-1, and 17-20 at.% for the AMPP-SPS specimens, Table 3-2. For the 19.8 at.% Hf specimen, this is indicated by point A in Figure 3-13(b). This position yields a higher volume fraction of the B1 γ -TaC phase.

Note that it was estimated that the VPS process lost less carbon than the AMPP-SPS process. The AMPP-SPS processed specimens formed nearly equivalent volume % of TaC and Ta₂C phases suggesting a possible carbon loss saturation transition. The stabilization effects of the HfC content were offset by a greater carbon loss. This analysis indicated that the VPS processed specimens benefited from the stabilizing effects of the increased HfC content while this stabilizing effect was offset by the AMPP-SPS processed specimens which had a higher carbon loss.

Further analysis on thermodynamic mobility of the various constituents addresses the possibility that carbon and hafnium are lost together. It has been reported that at approximately 2000°C, the vapor pressure of carbon is $\sim 3 \times 10^{-3}$ Pa (Figure 3-14), hafnium is $\sim 1 \times 10^{-2}$ Pa (Figure 3-15), and tantalum is $\sim 4 \times 10^{-6}$ Pa (Figure 3-16) [87]. Note, carbon and hafnium have vapor pressures much greater than tantalum's. In addition, Cowley and Mingqui [88] reported that the diffusion of hafnium to be greater than carbon in HfC. Valvoda *et al.* [89] reported that hafnium has a higher intrinsic diffusivity than tantalum in an HfC-TaC diffusion couple. This

suggests that at various temperatures throughout solidification, hafnium and carbon will have much higher mobility.

Additional work with the phase diagrams has shown that if carbon and hafnium are lost, the B1 γ -TaC phase will still be stabilized. As seen in Figure 3-13(b), the solid line indicates equal loss of carbon and hafnium. Further analysis showed that the decrease in hafnium along with carbon resulted in shorter tie lines which thermodynamically would cause the greater volume fraction of Ta₂C. However, the change in composition, because of hafnium loss, offsets this thermodynamic trend and stabilized the B1 γ -TaC phase, Table 3-3.

Table 3-3 Phase formation analysis for the 19.8 at.% HfC specimen based on phase diagram information at 1850°C [82] for a composition with 40 at.% carbon. The tie lines in Figure 3-13(b) for carbon (dashed line) and hafnium + carbon (solid line) loss were used to estimate phase %. See Appendix 7-5 for sample calculation.

Elemental Loss	Estimated Phase %	
	TaC	Ta ₂ C
Carbon	66	34
Carbon-Hafnium	69	31

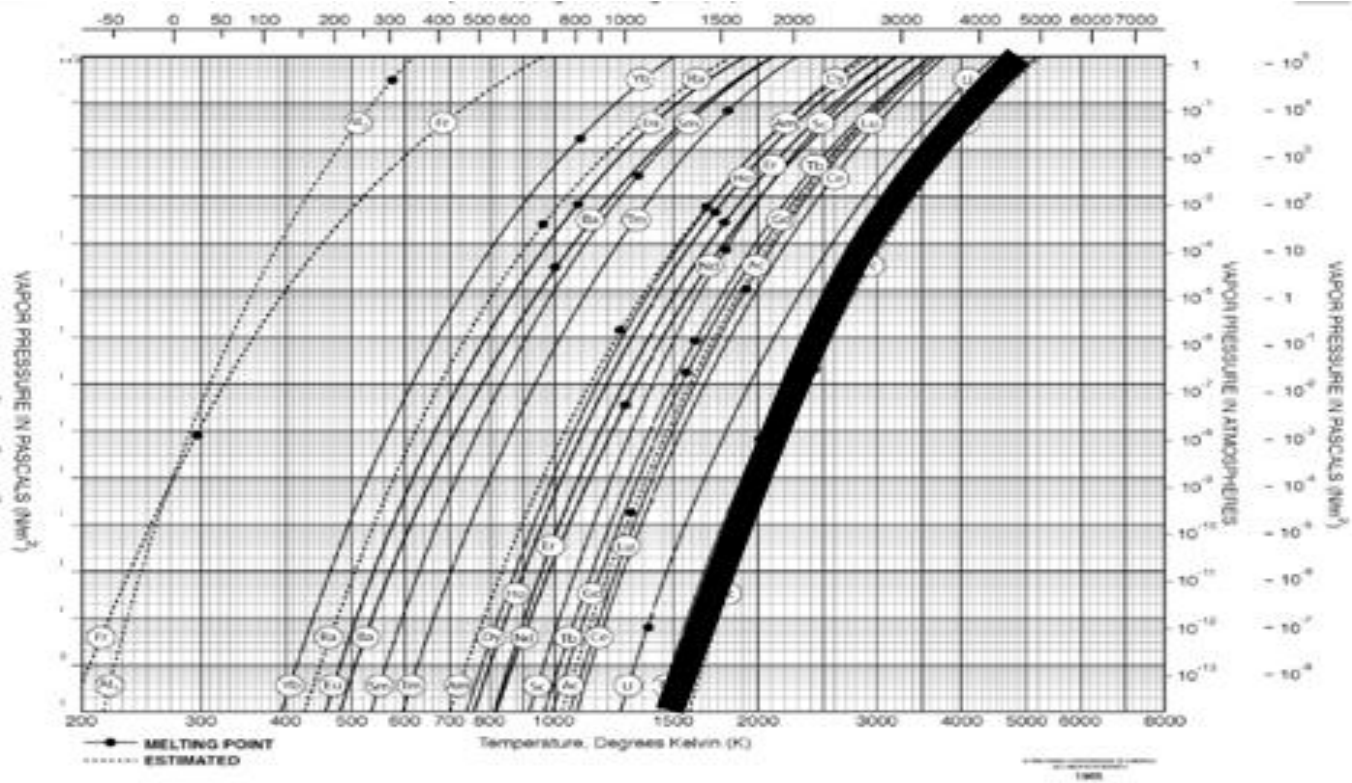


Figure 3-15 The vapor pressures for hafnium which is highlighted. [87]

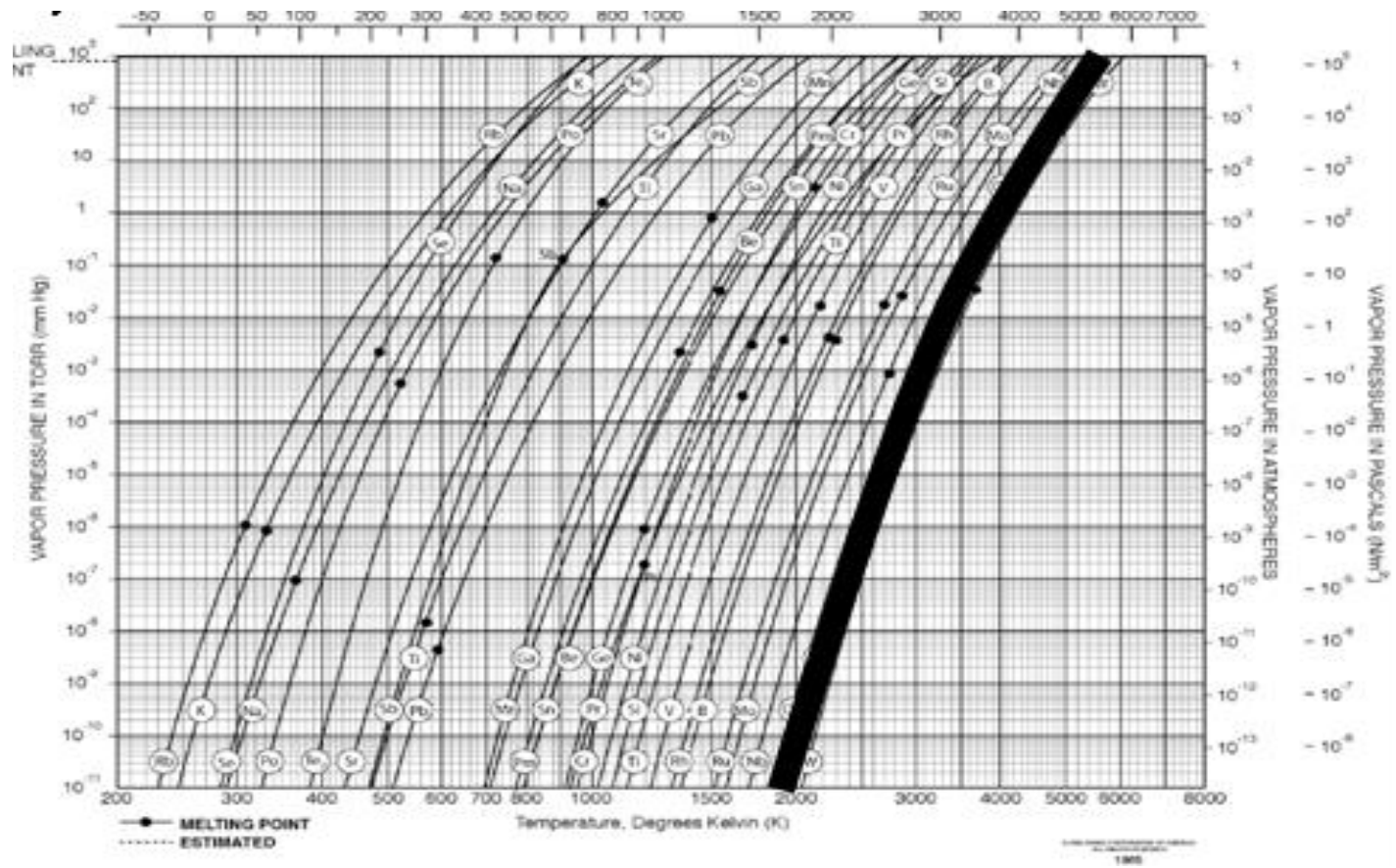


Figure 3-16 The vapor pressures for tantalum which is highlighted. [87]

This compositional effect of hafnium loss was investigated further. Assuming that the B1 γ -TaC phase is stabilized for larger ratios of carbon-to-metal (closer to 1 carbon :1 metal), equation (3) describes that ratio if hafnium and carbon are removed at a similar rate, and tantalum is not.

$$\frac{c}{M}(c, y, Hf_0) = \frac{(1-c)}{(1-Hf_0[c*y])} \quad (3)$$

where in equation (3) C/M is the carbon-to-metal ratio after processing, c is the % of carbon loss during processing, y is the ratio of hafnium to carbon loss, and Hf_0 is the initial value of HfC content. In the limiting cases of only TaC ($Hf_0 = 0$), the carbon-to-metal ratio clearly decreases and becomes metal rich with carbon loss; likewise, for only HfC ($Hf_0 = 1$) the carbon-to-metal ratio (C:M) is constant at 1:1 for equal carbon and hafnium loss ($y = 1$). In general, for increasing values of y and Hf_0 , the carbon-to-metal ratio approaches 1:1 and the B1 γ -TaC phase is stabilized. Figure 3-17 illustrates the carbon-to-metal relationship of equation (3) if carbon and hafnium are assumed to have the same loss rate ($y=1$). The contour lines represent different ratios of carbon-to-metal. For a process with 13% equivalent elemental loss across all initial HfC content (solid dark line in Figure 3-17), the carbon-to-metal ratio starts from 0.8:1 and approaches 0.9:1 as the initial HfC content increases (Note for 20% equivalent elemental loss the ratio starts at 0.75:1). Likewise, consider initial HfC contents of 3 and 20 at.% (similar to our experimental conditions). The 20 at.% initial HfC composition achieves a 0.8:1 ratio after approximately 20 % elemental loss as compared to the 3 at.% initial HfC specimen which achieved a 0.8:1 ratio after approximately 15% elemental loss. Thus, the B1 phase would be stabilized for higher initial HfC content.

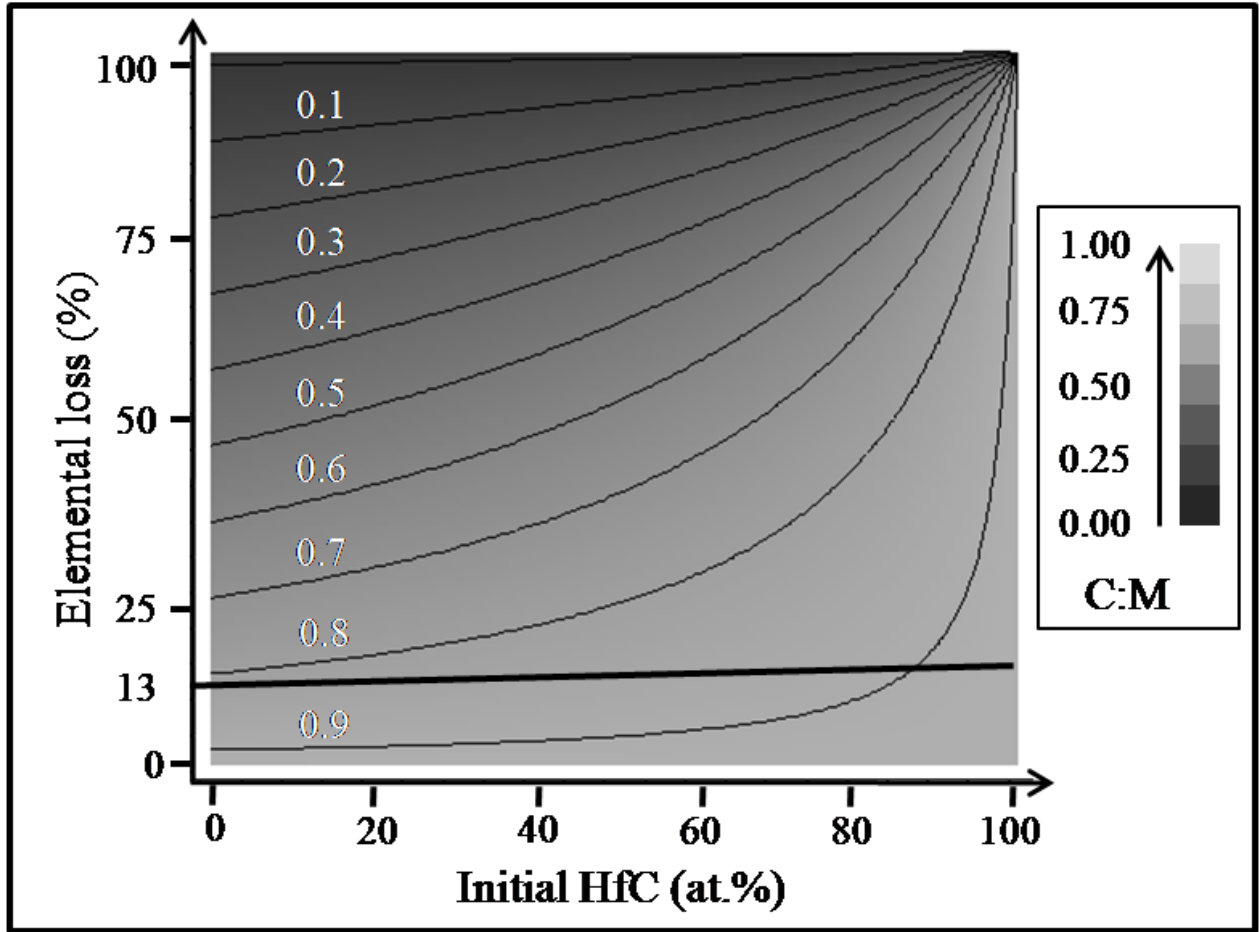


Figure 3-17 Effects of equivalent hafnium and carbon mobility during processing. The results are represented by a 2-D topography graph where the x-axis is initial $(\text{TaC})_{100-x}(\text{HfC})_x$ composition with respect to HfC content, the y-axis is hafnium and carbon elemental % loss, and the z-axis is the carbon-to-metal ratio after processing represented by contour lines. The approximation of 13 % elemental loss is represented by the bold line.

In summary, it should be noted that both thermodynamic components, chemical and compositional, are believed to contribute towards the phase formations found in the $(\text{TaC})_{100-x}(\text{HfC})_x$ system. This is clearly a complex process. It was first shown from the phase diagrams that the presence of initial hafnium, which does not form Ta-rich sub-stoichiometric phases, helped facilitate a greater tolerance for carbon deficiency in maintaining the B1 γ -TaC phase. This stabilizing effect was naturally altered by overall carbon loss. Additionally, the B1 γ -TaC phase could be stabilized if hafnium was lost along with carbon during the processing, as seen in the phase diagram tie lines. Lastly, it has been reported that hafnium has a higher mobility than tantalum in these carbide systems [87-89]. This would suggest it is feasible that the loss of the hafnium metallic atoms along with the carbon atoms could occur thereby maintaining the higher carbon-to-metal ratio which would ultimately stabilize the B1 γ -TaC phase.

Chapter 4 Fracture and Oxidation Behavior

4.1 VPS and AMPP-SPS Processed $(\text{TaC})_{100-x}(\text{HfC})_x$ Indentation Results

The results for hardness and indent behavior for the VPS processed specimens for the $(\text{TaC})_{100-x}(\text{HfC})_x$ system where X is 0.3, 3.0, 16.5, and 19.8 at.% are found in Table 4-1. The results for hardness and indent behavior for the AMPP-SPS processed specimens where X is 5.8, 10.7, 17.6, and 25.0 at.% are summarized in Table 4-2.

Table 4-1 Knoop indentation results for 200g load for the VPS processed specimens.

Nominal Composition $(\text{TaC})_{100-x}(\text{HfC})_x$	Mean Hardness	
	Indent (μm)	HK
0.3 at.%	46	1340 \pm 6%
3.0 at.%	63	720 \pm 7%
16.5 at.%	47	1310 \pm 8%
19.8 at.%	45	1430 \pm 7%

Table 4-2 Knoop indentation results for 200g load for the VPS processed specimens.

Nominal Composition $(\text{TaC})_{100-x}(\text{HfC})_x$	Mean Hardness	
	Indent (μm)	HK
5.8 at.%	48	1200 \pm 8%
10.7 at.%	47	1290 \pm 5%
17.6 at.%	46	1350 \pm 7%
25.0 at.%	46	1330 \pm 8%

4.1.1 Indent Behavior

Based on indent lengths, the overall Knoop value (HK) was found, Appendix 7-6. It was found that the indents formed by Knoop hardness at 200g decreased as HfC content increased.

This data also showed that the Knoop hardness values increase with increasing HfC content, with

the exception of the 0.3 at.% HfC specimen, suggesting possible greater fracture toughness for specimens with higher HfC content. Further SEM imaging of the VPS indent site revealed, Figure 4-1, that the lower hafnium content specimens, 0.3 and 3.0 at.% HfC, had a prevalence of cracks originating from the indentation site while the 16.5 and 19.8 at.% HfC specimens did not. Similar behavior was seen for the AMPP-SPS specimens, Figure 4-2, the lower (5.8 at.% HfC) specimen had multiple cracks propagation from the indentation site while the higher (10.7 – 25.0 at.% HfC) specimens had a decrease in crack propagation.

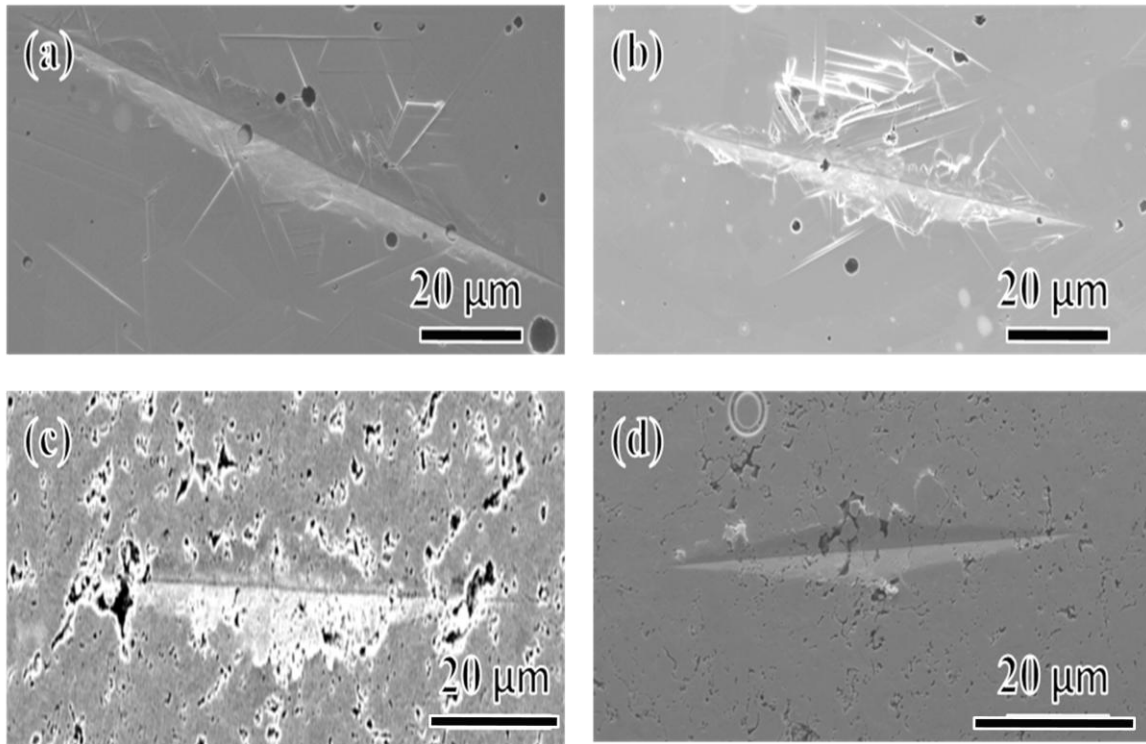


Figure 4-1 SEM electron imaging of indent behavior for VPS processed (a) 0.3, (b) 3.0, (c) 16.5, and (d) 19.8 at.% HfC specimens.

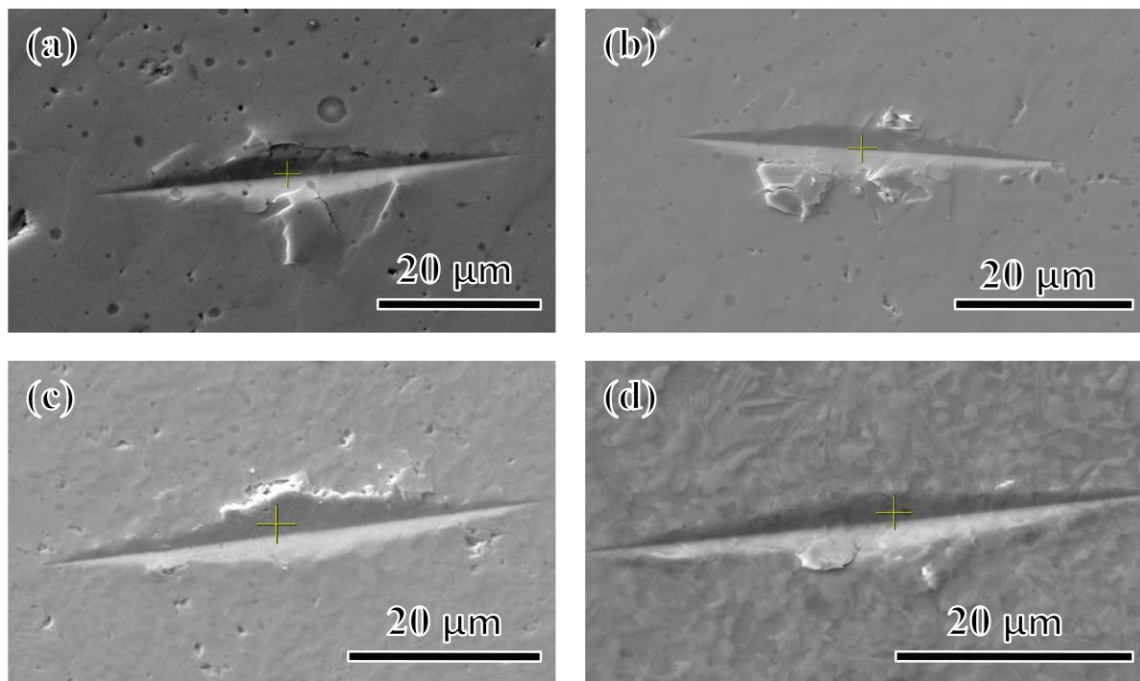


Figure 4-2 SEM electron imaging of indent behavior for AMPP-SPS processed (a) 5.8, (b) 10.7, (c) 17.6, and (d) 25.0 at.% HfC specimens.

4.1.2 Fracture Behavior Analysis

The VPS 0.3 at.% HfC specimen, has one of the highest hardness values, Figure 4-3. This specimen also has the highest Ta₄C₃ phase content than any other VPS specimen and the largest grain diameter. Research has found that the Ta₄C₃ phase has the hardest microhardness values [37], high fracture toughness, and high flexure strength [90]. Figure 4-4 plots the HfC contents for the VPS and AMPP-SPS processed specimens with respect to Ta₄C₃ phase volume %. This is suspected to be the reason for the high hardness value, though its grain size was large. The 3.0 at.% HfC specimen had a lower Ta₄C₃ volume fraction and lower HK value. Interestingly, the hardness values are recovered and increase for 5.8 – 25.0 at.% HfC specimens which have very low Ta₄C₃ phase content. To reconcile this observation, it is noted that the grain size also readily decreases over this HfC content region, between 1-3 μm for the 16.5 – 25.0 at.% HfC specimens. The lack of the strengthening effect from the Ta₄C₃ phase suggests that the low mean grain diameter values increase the hardness values since room temperature indents have been reported to have dislocations in tantalum carbides [48,80,81]. The smaller volume of each grain would be a strengthening mechanism.

In addition, it was observed that an increase in HfC content was related to the indent behavior near the Knoop indentation location, Figure 4-1 and Figure 4-2. The lower HfC content specimens had cracks propagate from the indent site while the higher HfC content specimens' crack propagation behavior diminished. The Ta₄C₃ phase is known to have crack propagation during deformation [37]. The loss of this phase could reduce its effect on the deformation mechanism under the indent.

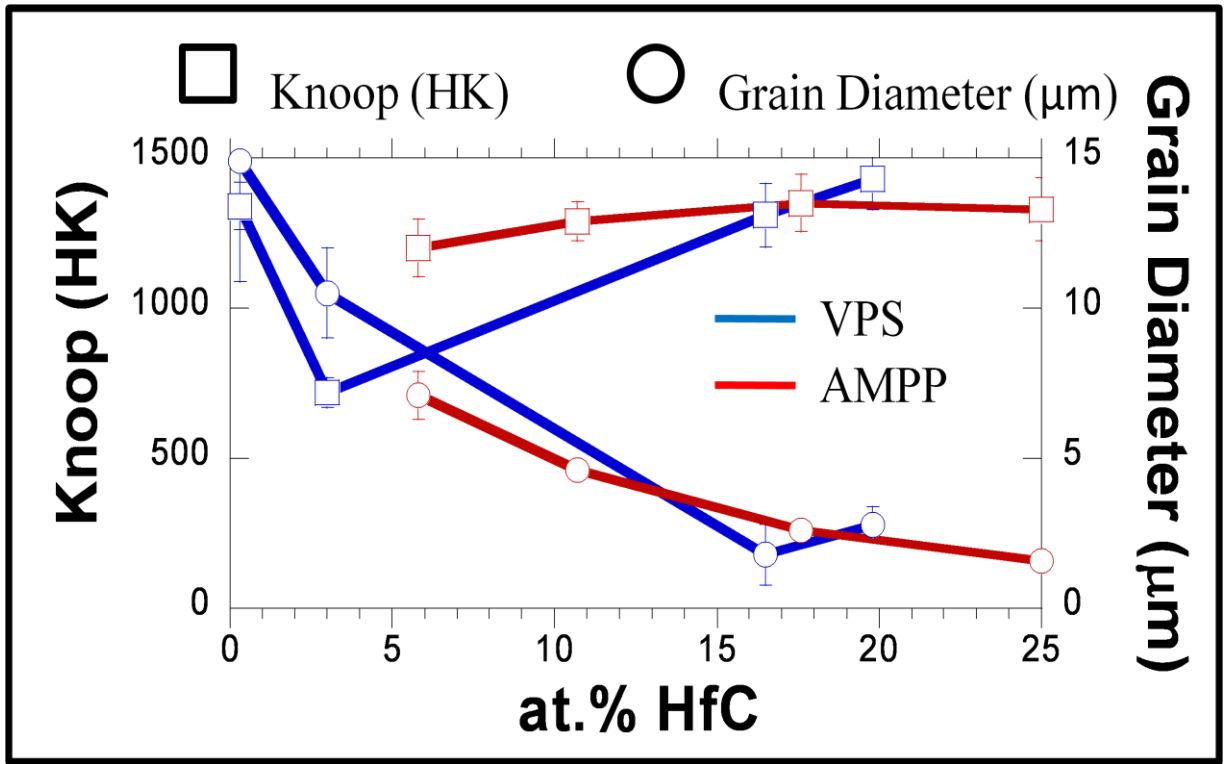


Figure 4-3 Plot of initial HfC content vs. mean grain diameter (μm) and Knoop value conducted at 200g for the VPS and AMPP-SPS processed specimens.

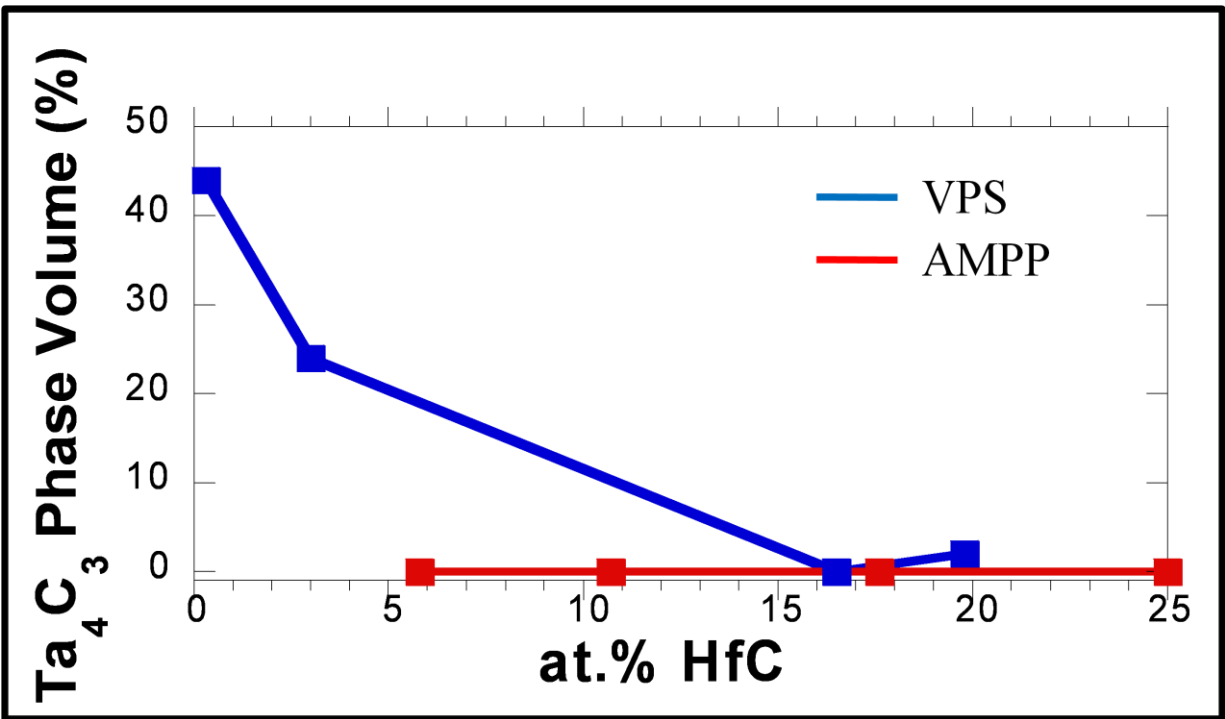


Figure 4-4 Plot of HfC content vs. Ta_4C_3 phase volume % for the VPS and AMPP-SPS processed specimens.

4.2 AMPP-SPS Processed Ta_{1-x}Hf_xC Oxidation Results

The results for oxidation behavior for the AMPP-SPS processed specimens for the (TaC)_{100-x}(HfC)_x system where X is 5.8, 10.7, 17.6, and 25.0 at.% are summarized in **Table 4-3**.

Table 4-3 Oxidation results for the AMPP-SPS processed specimens. Oxidation treatment conducted at 1000°C for 30 min.

Nominal Composition (TaC) _{100-x} (HfC) _x	Mean Mass Change			Mean Oxidation Thickness (μm)
	Initial (g)	Final (g)	%	
5.8 at.%	2.06	2.11	2.5	590
10.7 at.%	1.7	1.74	2.2	360
17.6 at.%	4.06	4.13	1.6	200
25.0 at.%	1.92	1.93	0.6	100

4.2.1 Oxide Phase Characterization

The XRD scans for the AMPP-SPS processed specimens show that the primarily oxide phase that formed during heat treatments is Ta₂O₅, Figure 4-5(a). It should be noted that the d-spacing data for multiple Ta₂O₅ and HfO₂ phases overlap, Figure 4-5(b); however, peak ID was based on the phases that were consistently closest in d-spacing values. This peak ID method labeled the following peaks: 2θ-23° hexagonal Ta₂O₅, 2θ-26.5° orthogonal Ta₂O₅, 2θ-28.5° hexagonal Ta₂O₅, and 2θ-30.5° orthogonal HfO₂ and highlighted yellow in Figure 4-5. The tetragonal HfO₂ was not identified.

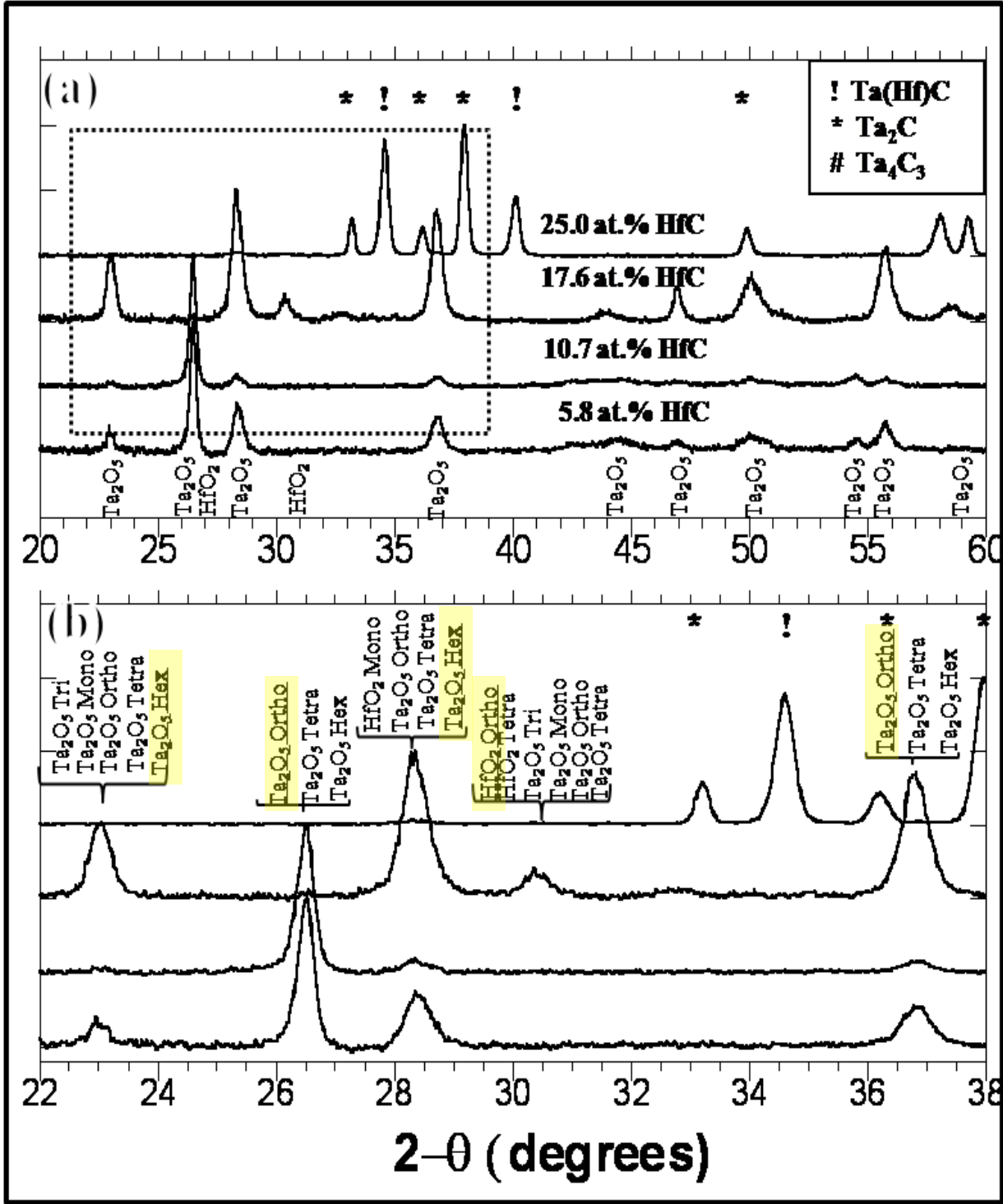


Figure 4-5 XRD results (a) from the AMPP-SPS processed 5.8, 10.7, 17.6 and 25.0 at.% HfC oxidized specimens at 1000°C for 30 min. Each spectra revealed the phases (b) Ta_2O_5 and HfO_2 at various diffracted intensities and crystallographic structures. Underlined/highlighted phases indicate closest in d-spacing.

4.2.2 Oxidation Behavior

The oxidation behavior of the AMPP-SPS specimens is analyzed by mass change %, oxide scale length, indent formation, and relative oxide scale adhesion. SEM micrographs, Figure 4-6, shows the oxide-carbide transition interface. As HfC content increased, the mass % decreased, Table 4-3. In addition, the SEM micrographs, Figure 4-7, for the $(\text{TaC})_{100-x}(\text{HfC})_x$ specimens indicated a reduction in scale thickness with respect to an HfC content increases, Table 4-3. An example of oxide mass % change and oxide scale thickness can be found in Appendix 7-7. Further observations of the oxide scale indicated transitional regions within the oxide scale, Figure 4-8, which are termed oxide scale and oxy-carbide. SEM imaging of the two regions indicate that they are separated by a crack interface. The crack and oxy-carbide region is greatest for the 5.8 at.% HfC sample and decreased in splitting width between the scale and matrix as HfC content increases.

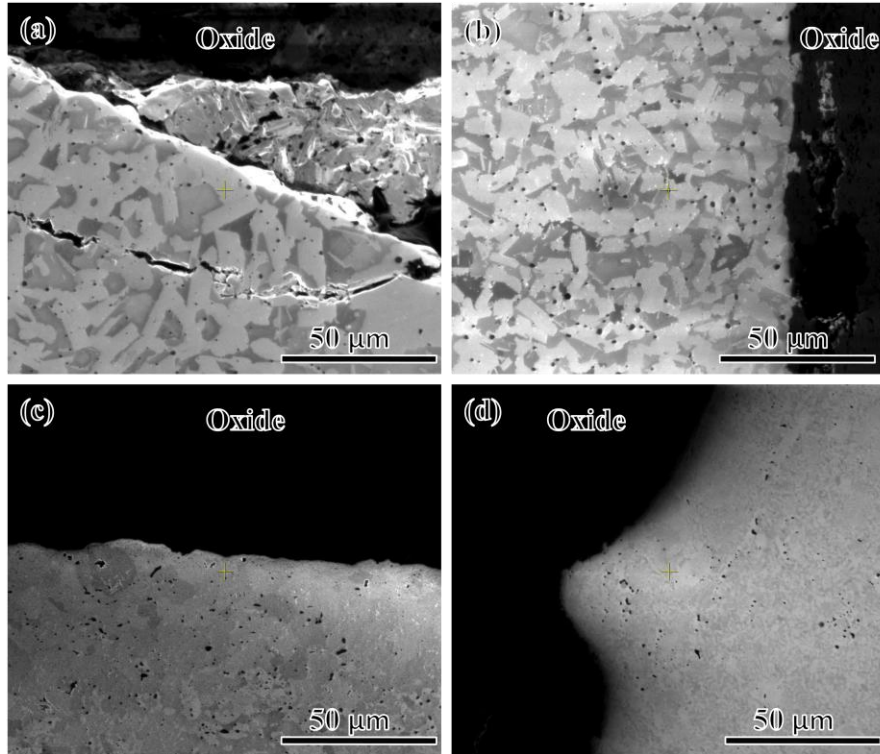


Figure 4-6 SEM-FIB ion contrast images of oxide, heat treated at 1000°C for 30 min, and bulk regions for the (a) 5.8, (b) 10.7, (c) 17.6, (d) and 25.0 at.% specimens.

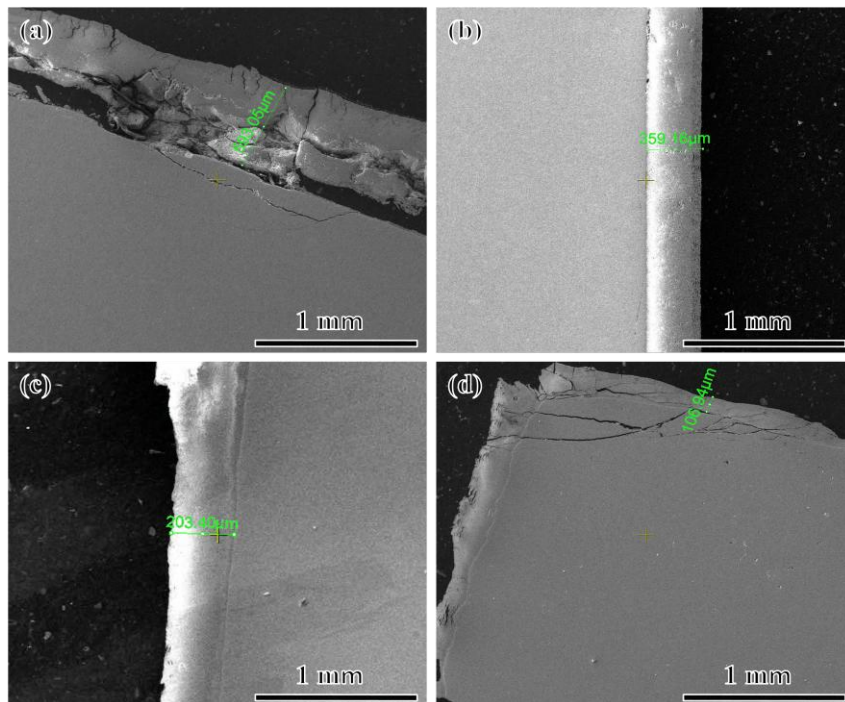


Figure 4-7 SEM-FIB ion contrast images showing the oxide scale length, heat treated at 1000°C for 30 min, for the (a) 5.8, (b) 10.7, (c) 17.6, (d) and 25.0 at.% specimens.

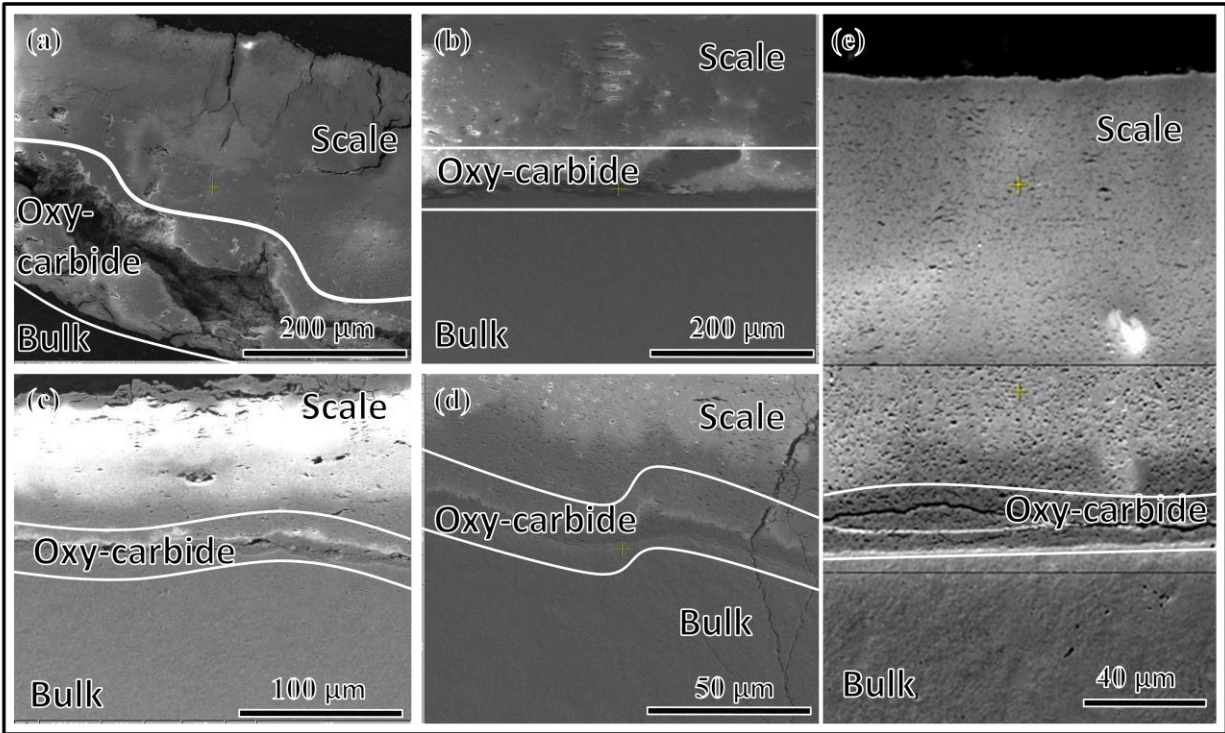


Figure 4-8 Representative SEM images of the specimens; 5.7 at.% HfC (a), 10.7 at.% HfC (b), 17.6 at.% HfC (c), and 25.0 at.% HfC (d) oxide scale transition, heat treated at 1000°C for 30 min. Composite image (e) of bulk to oxide transition for the 25.0 at.% HfC specimen.

To investigate the oxy-carbide interface, site-specific FIB lift outs of a TEM foil were performed. In particular, two regions of the scale were viewed: the scale itself and the transition zone between the scale and carbide, Figure 4-9. In addition, an SEM-EDS line scan, Figure 4-9(a), was conducted over the carbide-scale region and found that the C(K)/O(K) ratio dropped between the carbide interface and oxide interface. Previous research of HfC oxidation indicated an intermediate region between the carbide interface and oxide interface [91] characterized by an additional plateau. This was not observed. The additional plateau in ref [91] was found to be an oxy-carbide interlayer between the carbide and oxide. Characterized as the tetragonal HfO₂ phase this region demonstrated a decrease in oxide diffusion with respect to the main orthogonal HfO₂ oxide phase. The lack of an XRD identified tetragonal HfO₂ in this specimen along with the absence of an EDS plateau is consistent with this prior research findings [91]. The transition region for the AMPP-SPS processed specimen grains were acicular in morphology as shown in Figure 4-9(b-c). In contrast, the non oxide grains in the matrix were equiaxed. The oxidation not only changes the phase but the grain morphology. Hafnium inclusions were found in the TEM transitional foil indicated by EDS data, Figure 4-9(b).

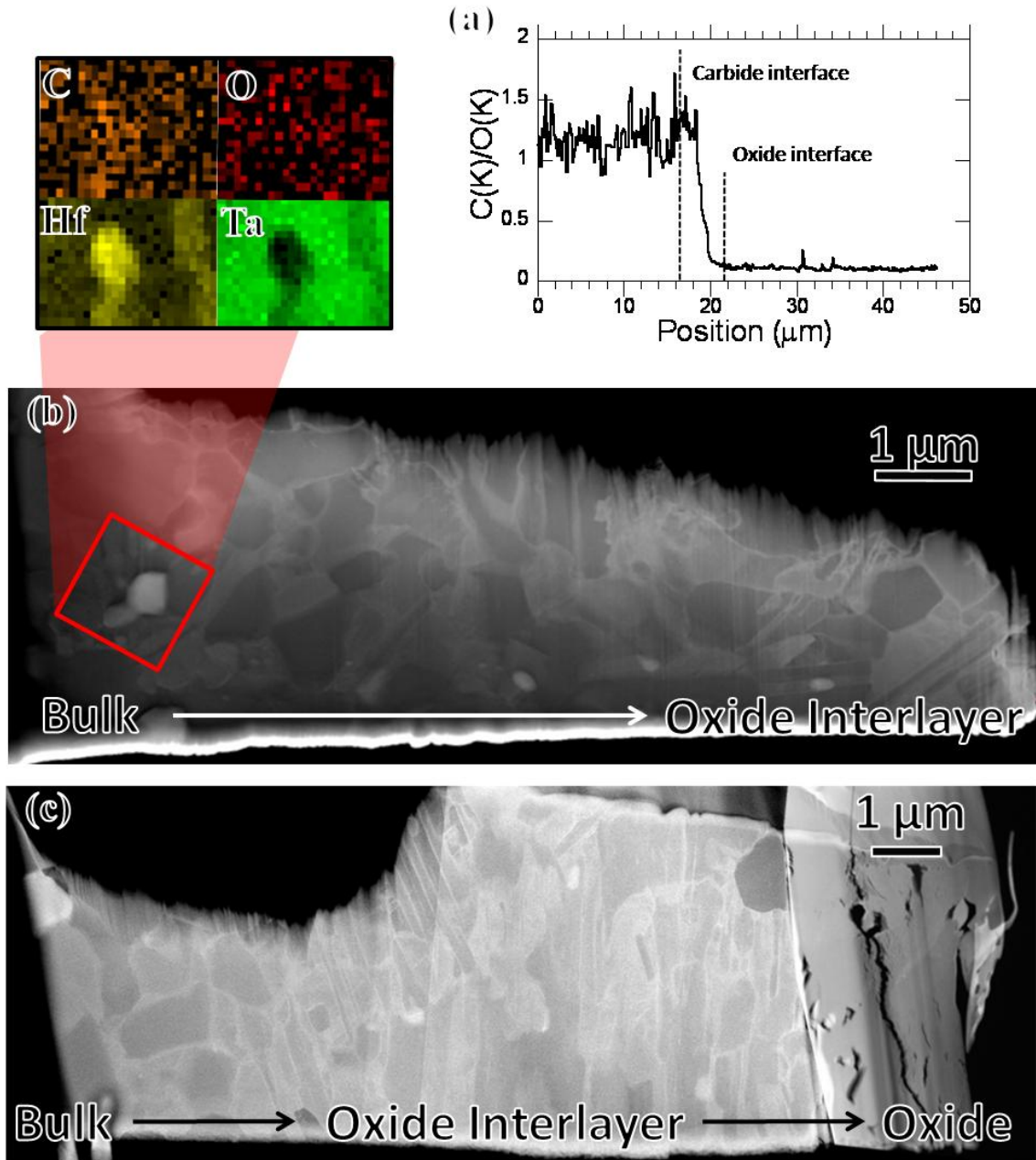


Figure 4-9 SEM-EDS (a) results of C(K)/O(K) vs. position from carbide to oxide scale. Representative STEM-HAADF composite images of 25.0 at.% HfC (b) from carbide to oxide interlayer with EDS mapped region and (c) from carbide to oxide.

4.2.3 Oxidation Analysis

In general, it was found that the addition of HfC content to the AMPP-SPS processed specimens improved oxidation resistance at 1000°C. The increase in HfC content reduced the crack splitting between the oxide scale and matrix along the carbide-oxy carbide interface, Figure 4-8. The oxide scale also decreased in thickness for equivalent exposures with increasing HfC content, Table 4-3. The oxide scale morphology qualitatively had less cracks with increasing HfC content, compare Figure 4-8(a) to Figure 4-8(e). The decrease in cracks along the oxide scale interface suggests an improved oxide scale adhesion and an improvement in ablation resistance. The decrease in oxide scale is a direct correlation with oxidation resistance.

It is interesting to note that the grains in the STEM-HAADF images of the oxide interlayer, Figure 4-9(b-c), are primarily acicular when the majority of the bulk grains are primarily equiaxed, Figure 4-6. The change in crystal symmetry from cubic (carbide phase) to orthorhombic or monoclinic (oxide phases) contributes to a morphology change. Furthermore, these grain boundaries are brighter in contrast than the interior grain boundaries suggesting that these grain boundaries are rich in hafnium; EDS results indicated hafnium clusters in the microstructure. It is possible that hafnium is diffusing along grain boundaries into the oxide scale thus improving the oxidation behavior.

The presence of separate Ta-oxide and Hf-oxide phases would indicate little to no mixing of metal species to each other's scale. The oxidation improvement is primarily driven by the formation of HfO₂ which is known to exhibit better oxidation behavior. Interestingly, the region between the matrix and oxide scale exhibits a different contrast, suggestive that some peculiar mixing phase interactions are occurring and would be suggested for future work. The lack of the

tetragonal HfO₂ phase suggests improvements are still possible. The tetragonal phase forms at approximately 1400-1500°C, which is higher than the temperatures studied.

Chapter 5 Conclusion

5.1 Major Findings

The VPS and AMPP-SPS processed specimens showed that an increase in at.% of HfC content in the $(\text{TaC})_{100-x}(\text{HfC})_x$ system resulted in:

- The reduction of grain size. The smaller grain size is contributed to a depressed melting temperature caused by the addition of HfC content and carbon loss during processing. This depressed melting temperature facilitated a higher nucleation density that lead to the finer grain size.
- An increase in porosity. The formation of finer grain size led to numerous grains being contracted from each other during solidification. This drastic volume change led to voids and an increase in porosity.
- The stabilization of a higher volume fraction of TaC. The formation of the sub-stoichiometric, tantalum-rich phases at lower HfC contents was rationalized from the carbon loss intrinsic to processing. Conversely, if the HfC content is sufficiently high, the effect of carbon depletion is offset by the stabilization of the TaC phase by HfC. Similarly, if hafnium and carbon are simultaneously lost, the TaC phase will still be stabilized.
- Increased micro hardness. It was observed that multiple mechanisms contributed towards micro hardness. The presence of the Ta_4C_3 phase contributed to increased

micro hardness values. The formation of small fine grains led to a second strengthening mechanism.

- Increased oxidation resistance. The HfC additions caused the formation of a Ta₂O₅ and HfO₂ oxide mixed interface which reduced crack density and overall oxide scale thickness. It was observed that this oxide mixture caused a grain morphology change.

5.2 Future Work

Future work can focus on the mechanical relationships between the microstructure and additives for oxidation and non oxidation behavior. Some suggested topics are:

- How does carbon loss affect the resulting properties at various stages during processing?
- How do other transitional metals from groups IV and V affect the Ta-C system for oxidation and non oxidation behavior?
- What are the effects of hafnium carbides and small grains on tantalum carbide dislocation slip?
- How does hafnium content effect the oxidation behavior of the system at higher oxidation temperatures and at what parameters will the tetragonal HfO₂ phase form?

Chapter 6 References

- [1] M.J. Gasch, D.T. Ellerby and S.M. Johnson, "Ultra High Temperature Ceramic Composites." *Handbook of Ceramic Composites*, 197-224 (2005).
- [2] E. Wuchina, E. Opila, M. Opeka, W. Fahrenholtz and I. Talmy, "UHTCs: Ultra-High Temperature Ceramic Materials for Extreme Environment Applications." *The Electrochemical Soc.*, 30-36 (2007).
- [3] W. Fahrenholtz and G.E. Hilmas, "Ultra-High Temperature Ceramics - An Introduction to Ultra-High Temperature Ceramics." Missouri University of Science and Technology. AZoM.com, 2010.
- [4] S.T. Oyama, "The Chemistry of Transition Metal Carbides and Nitrides." Chapman and Hall, London, UK, 1996.
- [5] V.A. Guanov, A.L. Ivanovsky and V.P. Zhukov, "Electronic Structure of Refractory Carbides and Nitrides." Cambridge University Press, Cambridge, UK, 1994.
- [6] J.F. Shackelford and W. Alexander, "Thermal Properties of Materials." CRC Press LLC, 2001.
- [7] E.F. Westrum and G. Feick, "Zirconium Carbide: Heat Capacity and Thermodynamic Properties from 5 to 350K." *J. Chem. and Eng. Data*, 2 [8] (1963).
- [8] ULTRAMET - Ceramic Protective Coatings. *ULTRAMET Advanced Materials Solutions*. [Online] 2010. [Cited: November 10, 2010.] http://www.ultramet.com/ceramic_protective_coatings.html.
- [9] K. Kelley, "The Specific Heats at Low Temperatures of Tantalum Oxide and Tantalum Carbide."; in Metallurgical Division, Bureau of Mines, Metallurgical Fundamentals Section, United States Department of the Interior, [62] 818-819 (1940).
- [10] A. Roine, *HSC Chemistry 5.11*. Pori, Finland : outokumpu Research Oy.
- [11] C. Kim, G. Gottstien, and D.S. Grummon., "Plastic flow and dislocation structures in tantalum carbide: Deformation at low and intermediate temperatures." *Acta metal. Mater.*, 7 [42] 2291-2301 (1994).

- [12] A.T. Santhanam, "Application of transition metal carbides and nitrides in industrial tools"; in *The Chemistry of Transition Metal Carbides and Nitrides* by S. T. Oyama. Chapman and Hall, London, UK, 1996.
- [13] X. Zhang, P. Hu, J. Han, L. Xu and S. Meng "The addition of lanthanum hexaboride to zirconium diboride for improved oxidation resistance." *Scripta Mat.*, [57] 1036-1039 (2007).
- [14] S. Shimada and T. Sata, "Preparation and high temperature oxidation of SiC compositionally graded graphite coated with HfO₂." *Carbon*, [40] 2469-2475 (2002).
- [15] S. Shimada, K. Nakajima and M. Inagaki, "Oxidation of single crystals of hafnium carbide in a temperature range of 600 to 900 C." *J. Am. Ceram. Soc.*, [80] 1749-1756 (1997).
- [16] W. Han, P. Hu, X. Zhang J. Han and S. Meng, "High-Temperature oxidation at 1900C of ZrB₂-xSiC ultrahigh-temperature ceramic composites." *J. Am. Ceram. Soc.*, [91] 3328-3334 (2008).
- [17] S. Scholz, "Some new aspects of hot pressing of refractories." Academic Press Inc., New York, NY, 1962. *Special Ceramics 1962 Proceedings of a Symposium held by the British Ceramic Research Association.* pp. 293-307.
- [18] X. Zhang, G.E. Hilmas, W. G. Fahrenholtz, and D. M. Deason., "Hot Pressing of Tantalum Carbide with and without Sintering Additives." *J. Am. Ceram. Soc.*, 2 [90] 393-401 (2007).
- [19] E. Klerk and M. Roeder, "Studies with the electron-beam microanalyzer on hot-pressed tantalum carbide having small additions of manganese and nickel." *Z. Metallkunde*, [54] 462-470 (1963).
- [20] J.J. Fischer, "Hot-pressing mixed carbides of Ta, Hf, and Zr." *Ceram. Bull.*, 3 [43] 183-185 (1964).
- [21] L. Ramqvist, "Hot pressing of metallic carbides." *Powder Metall.*, 17 [9] 26-46 (1961).
- [22] W.C. Ruoff and A.L. Yohe, "Ultrafine-grain tantalum carbide by high pressure. Hot Pressing." *Ceram. Bull.*, 12 [57] 647-651 (1978).
- [23] M.H. Becher and P.F. Leibold, "Pressure-densification in tantalum carbide." *Ceram. Bull.*, 7 [49] 647-651 (1970).
- [24] J.X. Liu, Y.M. Kan, and G.J. Zhang, "Pressureless Sintering of Tantalum Carbide Ceramics without Additives." *J. Am. Ceram. Soc.*, 2 [93] 370-373 (2010).
- [25] S. Gupta, D. Filimonov, and M.W. Barsoum, "Isothermal Oxidation of Ta₂AlC in Air." *J. Am. Ceram. Soc.*, 9 [89] 2974-2976 (2006).

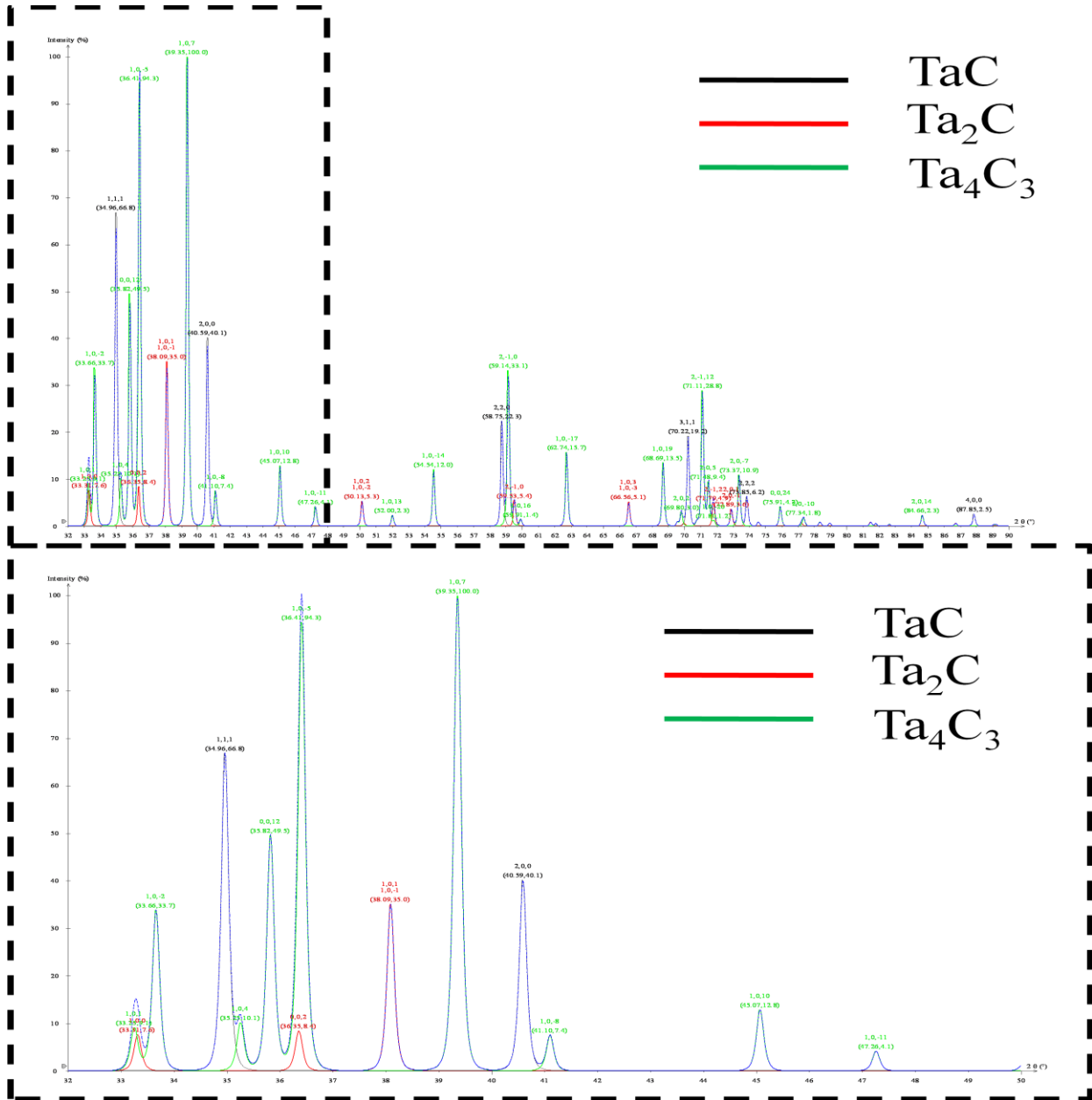
- [26] R.A. Andrievskii, N.S. Strel'nikova, N.I. Poltoratskii, E.D. Kharkhardin and V.S. Smirnov, "Melting point in systems ZrC-HfC, TaC-ZrC, TaC-HfC." *Powder Metall. Met. Ceram.*, 6 [10] 65-67 (1967).
- [27] G. Santoro and H.B. Probst, "An explanation of microstructures in the Tantalum-Carbon System."; in *Advances in X-ray Analysis*. Plenum Press, New York, NY, 1963, Vol. 12th Annual Conference.
- [28] E.K. Storms, "The Tantalum-Tantalum Carbide System."; in *The Refractory Carbides*, Academic Press, 1967.
- [29] R.A. Morris, "Characterization of the Microstructural Formations and Phase Transformation Pathways in Tantalum Carbides Dissertation." University of Alabama, Tuscaloosa, Al, 2010.
- [30] G.V. Rukina and V.B. Samsonov, "Microhardness and Electrical resistance of Tantalum Carbides in their Homogeneous Region." *Dopovidi Akad.*, 3 247 (1957).
- [31] V.L. Ormont and B.F. Smirnova, "Limits of Homogeneity and the Relation of the Thermodynamic and Other Properties of the Carbide Phases of Ta to Their Composition and Structure." *Zh. Fiz. Khim.*, [30] 1327 (1956).
- [32] V.L. Ormont and B.F. Smirnova, "Relation of the Heat and Free Energy of Formation of Tantalum Carbides to Phase and Chemical Composition." *Dokl. Akad.*, [100] 127 (1955).
- [33] R.T. Dolloff, "Research Study to Determine the Phase Equilibrium Relations of Selected Metal Carbides at High Temperatures."; in *National Carbon Research Laboratory Progress Report No. 3*. 1962. pp. 13-17.
- [34] R. Breuer and G. Lesser, "Carbide Phases in Tantalum." *Z. Metallk.*, [49] 622 (1958).
- [35] A.L. Bowman, "The Variation of Lattice Parameters with Carbon Content of Tantalum Carbide." *J. Phys. Chem.*, [65] 1596 (1961).
- [36] A.L. Giorgi, "Effect of Composition on the Superconducting Transition Temperature of Tantalum Carbide and Niobium Carbide." *Phys. Rev.*, 3 [125] 837 (1962).
- [37] G. Santoro, "Variation of Some Properties of Tantalum Carbide with Carbon Content."; in *Transactions of the Metallurgical Society of AIME*. 1963 pp. 1361-1368.
- [38] "Tantalum Oxide 21-1199."; in *JCPDS-International Centre for Diffraction Data*. 2009.
- [39] "Tantalum Oxide 33-1390."; in *JCPDS-International Centre for Diffraction Data*. 2009.
- [40] "Tantalum Oxide 25-0922."; in *JCPDS-International Centre for Diffraction Data*. 2009.
- [41] "Tantalum Oxide 18-1304."; in *JCPDS-International Centre for Diffraction Data*. 2009.

- [42] "Tantalum Oxide 27-1447."; in *JCPDS-International Centre for Diffraction Data*. 2009.
- [43] X. Zhang, G.E. Hilmas, and W.G. Fahrenholtz, "Densification, Mechanical Properties, and Oxidation Resistance of TaC-TaB₂ Ceramics." *J. Am. Ceram. Soc.*, 12 [91] 4129-4132 (2008).
- [44] B. Bargeron and J. Phillips, "Oxidation Mechanisms of Hafnium Carbide and Hafnium Diboride in the Temperature Range 1400 to 2100 C." *Tech. Digest*, 1 [14] 29-35 (1993).
- [45] B. Bargeron and J. Phillips, "Oxidation of Hafnium Carbide in the Temperature Range 1400 to 2060 C." *J. Am. Ceram. Soc.*, 4 [76] 1040-1046 (1993).
- [46] K. Frisk, "Carbon-Tantalum Binary Diagram."; in *ASM Alloy Phase Diagrams Center*. ASM International, 1996.
- [47] "TaC 00-035-0801."; in *JCPDS-International Centre for Diffraction Data*. 2009.
- [48] V.N. Gusev and A.I. Lipatnikov, "Atomic-Vacancy Ordering in the Carbide Phase Ta₄C_{3-x}." *Phy. of Solid State*, 9 [48] 1634-1645 (2006).
- [49] "Ta₂C 01-071-2677." ."; in *JCPDS-International Centre for Diffraction Data*. 2009.
- [50] H. Okamoto, "Carbon-Hafnium Binary Diagram."; in *ASM Alloy Phase Diagrams Center*. ASM International, 2001.
- [51] D. Ferro, J.V. Rau, V.R. Albertini, A. Generosi, R. Teghil and S.M. Barinov, "Pulsed Laser Deposited Hard TiC, ZrC, HfC and TaC films on Titanium: Hardness and an Energy-Dispersive X-Ray Diffraction Study." *Surf. Coat. Tech.*, [202] 1455-1461 (2008).
- [52] D. Ferro, S.M. Barinov, J.V. Rau, A. Latini, R. Scadurra and B. Brunetti, "Vickers and Knoop Hardness of Electron Beam Deposited ZrC and HfC Thin Films on Titanium." *Surf. Coat. Tech.*, [200] 4701-4707 (2006).
- [53] , "Hafnium Oxide 06-0318."; in *JCPDS-International Centre for Diffraction Data*. 2009.
- [54] , "Hafnium Oxide 81-0028."; in *JCPDS-International Centre for Diffraction Data* 2000.
- [55] , "Hafnium Oxide 90-04144."; in *JCPDS-International Centre for Diffraction Data*. 2009.
- [56] S.Z. Nazarova, E.Z. Kurmaev, N.I. Medvedeva, and A. Mowes, "Physical Properties and Electronic Structure of TaC-HfC Solid Solutions." *Russ. J. of Inorganic Chem.*, 2 [52] 233-237 (2007).
- [57] D.L. Deadmore, "Vaporization of Tantalum-Carbide-Hafnium-Carbide Solid Solutions at 2500 to 3000 K."; in National Aeronautics and Space Administration Report, Washington, D.C, 1964.

- [58] W-B. Han, P. Hu, X-H. Zhang, J-C. Han and S-H. Meng, "High-Temperature Oxidation at 1900C of ZrB₂-xSiC Ultrahigh Temperature Ceramic Composites." *J. Am. Ceram. Soc.*, 10 [91] 3328-3334 (2008).
- [59] M. Moldovan, C.M. Weyant, D.L. Johnson and K.T. Faber, "Tantalum Oxide Coatings as Candidate Environmental Barriers."; in Conference Proceedings, ASM International, 2003.
- [60] G. Guillermet and A.F. Grimvall, "Phase Stability Properties of Transition Metal Diborides." *Am. Inst. of Phys.*, 423-430 (1991).
- [61] L. Silvestroni, D. Sciti and A. Bellosi, "Microstructure and Properties of Pressureless Sintered HfB₂-Based Composites with Additions of ZrB₂ or HfC." *Adv. Eng. Mat.*, 10 [9] 915-920 (2007).
- [62] , "HfC 00-039-1491."; in *JCPDS-International Centre for Diffraction Data 2009*.
- [63] K. Balani, G. Gonzalez and A. Agarwal, "Synthesis, microstructure characterization, and mechanical property evaluation of vacuum plasma sprayed tantalum carbide." *J. Am. Ceram. Soc.*, 4 [89] 1419-1425 (2006).
- [64] T. Wooldrich and M.S. Kim, "Catalytically Assisted Self-Propagating High-Temperature Synthesis of Tantalum Carbide Powders." *J. Am. Ceram. Soc.*, 5 [84] 976-982 (2001).
- [65] H. Hutchings and I.M. Chen, "Abrasive wear resistance of plasma-sprayed tungsten carbide-cobalt coatings." *Surf. Coat. Technol.*, [61] 106-114 (1998).
- [66] C. Tendero, T. Christelle, T. Pascal, J. Desmaison and P. Leprince, "Atmospheric Pressure Plasmas: A Review." *Spectrochimica Acta Part B: Atomic Spectroscopy.*, 1 [61] 2-30 (2006).
- [67] S-J. L. Kang, "Sintering: Densification, grain growth and microstructure." Elsevier Press, Boston, 2005.
- [68] W.H. Guo and J.K. Tuan, "Multiphased ceramic materials: processing and potential." Springer, 2004.
- [69] R.B. Srinivasa, V. Musaramthota, D. Lahirir, V. Singh, S. Seal and A. Agarwal, "Spark plasma sintered tantalum carbide: Effect of pressure and nano-baron carbide addition on microstructure and mechanical properties." *Mat. Sci. Eng. A*, [528] 1287-1295 (2011).
- [70] R.B. Srinivasa, V. Musaramthota, D.A. Virzi, A.K. Keshri, D. Lahiri, V. Signh, S. Seal and A. Agarwal, "Spark plasma sintered tantalum carbide-carbon nanotube composite: Effect of pressure, carbon nanotube length and dispersion technique on microstructure and mechanical properties." *Mat. Sci. and Eng. A*, [528] 2538-2547 (2011).

- [71] R.E. Wilde and G. Palmer, "Mechanical Properties of Nanocomposite Materials." Elsevier Ltd., 2008.
- [72] E.R. Weibel, "Stereological Methods." Academic Press/Harcourt Brace Jovanovich, New York, NY, 1989. p. 339.
- [73] "Hafnium Oxide 08-0342."; in *JCPDS-International Centre for Diffraction Data*. 2009.
- [74] "Hafnium Oxide 78-00049."; in *JCPDS-International Centre for Diffraction Data*. 2009.
- [75] "Hafnium Oxide 78-0049."; in *JCPDS-International Centre for Diffraction Data*. 2009
- [76] D.B. Carter and C.B. Williams, "Transmission Electron Microscopy: a Textbook for Materials Science." Springer Science, New York, NY, 1996.
- [77] L.A. Giannuzzi, "Reducing FIB Damage Using Low Energy Ions." *J. of Microscopy and Microanalysis*, 2 [12] 1260-1261 (2006).
- [78] L.A. Giannuzzi, R. Geurts and J. Ringnalda, "2 keV Ga⁺ FIB Milling for Reducing Amorphous Damage in Silicon." *J. Microscopy and Microanalysis*, 2 [11] 828-829 (2005).
- [79] G.D. Quinn, "Hardness Testing of Ceramics." *Adv. Mat. and Proc.*, 2 [154] (1998).
- [80] D.J. Rowcliffe, "Structure of Non-Stoichiometric TaC." *Mat. Sci. Eng.*, [18] 231-238 (1975).
- [81] A.I. Gusev, A.S. Kurlov and V.N. Lipatnikov, "Atomic and vacancy ordering in carbide Ta₄C_{3-x} and phase equilibria in the Ta-C system." *J. Solid State Chem.*, [180] 3234-3246 (2007).
- [82] E. Rudy, Ruetter and H. Nowotny, "Carbon-Hafnium-Tantalum Ternary Alloy Phase Diagram (based on 1963 Rudy E.)."; in ASM Alloy Phase Diagrams Center. ASM International, 2006, Diagram # 955045.
- [83] V.S. Emel'yanov, A.I. Evstyukhin, V.G. Godin, G.I. Solovyev and S.A. Kokhtev, "Carbon-Hafnium-Tantalum Ternary Alloy Phase Diagram (based on 1967 Emel'yanov V.S.)."; in ASM Alloy Phase Diagrams Center. ASM International, 2006, Diagram # 955043.
- [84] T.F., Fedorov, "Carbon-Hafnium-Tantalum Ternary Alloy Phase Diagram (based on 1965 Fedorov T.F.) 1000C."; in ASM Alloy Phase Diagrams Center, 2007.
- [85] V.S. Emel'yanov, A.I. Evstyukhin, Y.G. Godin, G.I. Solovyev and S.A. Kokhtev, "Carbon-Hafnium-Tantalum Ternary Alloy Phase Diagram (based on 1967 Emel'yanov V.S.) 1500C."; in ASM Alloy Phase Diagrams Center, 2007.

- [86] D.V. Ragone, "Thermodynamics of Materials." John Wiley and Sons, New York, NY, 1995, Vol. II, pp. 146,179.
- [87] E.R. Honig, "Vapor pressure data for the solid and liquid elements." *RCA Rev.*, 30 [2] 285-305 (1969).
- [88] L. Cowley and J. Mingqui, "Hafnium carbide growth behavior and its relationship to the dispersion hardening in tungsten at high temperatures." *Mat. Sci. .Eng.*, [A160] 159-167 (1993).
- [89] V. Valvoda, L. Dobiasova and P. Karen, "X-ray diffraction analysis of diffusional alloying of HfC and TaC." *J. Mat. Sci.*, [20] 3605-3609 (1985).
- [90] L. Limeng, Y. Feng and Z. Yu, "Microstructure and Mechanical properties of spark plasma sintered TaC_{0.7} Ceramics." *J. Am. Ceram. Soc.*, 10 [93] 2945-2947 (2010).
- [91] C.B. Benson and R.C. Barger, "X-Ray Microanalysis of a Hafnium Carbide Film Oxidized at High Temperature." *Surf. and Coat. Technol.*, [36] 111-115 (1988).



Appendix 7-1 Example XRD identification template for the Ta-C system. CaRIne Crystallographic software was used.

2Theta	Radians	D Spacing	Intensity	Normalization	TaC	Ta2C	Ta4C3
33.1	0.577704	2.704141	39.28003	0.053018284		100	
34.68	0.60528	2.584474	740.877	1	111		111
36.1	0.630064	2.486003	37.6378	0.050801686		002	
37.9	0.66148	2.371969	122.5295	0.165384406		011	
40.3	0.703368	2.236072	554.0748	0.747863415	200		200
50	0.872665	1.822638	24.79236	0.033463527		102	211
58.52	1.021367	1.575945	311.1641	0.419994254	220		220
66.38	1.15855	1.407117	31.37201	0.042344428		103	
69.9	1.219985	1.344618	428.1087	0.577840534	311	200	311
71.42	1.246514	1.319689	53.15347	0.071743985		112	
73.44	1.28177	1.288298	141.7384	0.191311726	222		
87.46	1.526465	1.114312	69.72844	0.094116086	400		
95.28	1.66295	1.042432	28.75918	0.03881775			
97.76	1.706234	1.022495	180.4289	0.243534204	331		
101.14	1.765226	0.997254	220.8664	0.298114767	420		
105.26	1.837134	0.969232	24.90461	0.033615037			421
112.1	1.956514	0.928579	33.29618	0.04494158			
115.82	2.02144	0.909191	184.2056	0.248631853	422		
118.06	2.060536	0.898352	26.4593	0.035713489			

Peak data from peak analyzing software: Origins

Origins Software able to de-convolute double peaks

TaC Peak No.	2Theta	Radians	sin2θ	sin2θ/3	sin2θ/4	sin2θ/8	sin2θ/K	h2+k2+l2	hkl
1	34.68	0.60528	0.088829	0.029609549	0.022207	0.011104	2.989573	3	111
2	40.3	0.703368	0.118666	0.039555278	0.029666	0.014833	3.993759	4	200
3	58.52	1.021367	0.2389	0.079633182	0.059725	0.029862	8.040286	8	220
4	69.9	1.219985	0.32817	0.109390051	0.082043	0.041021	11.04473	11	311
5	73.44	1.28177	0.35749	0.119163456	0.089373	0.044686	12.03152	12	222
6	87.46	1.526465	0.477842	0.159280526	0.11946	0.05973	16.082	16	400
7	97.76	1.706234	0.567512	0.189170644	0.141878	0.070939	19.0999	19	331
8	101.14	1.765226	0.596603	0.198867832	0.149151	0.074575	20.07899	20	420
9	115.82	2.02144	0.717773	0.239257557	0.179443	0.089722	24.15701	24	422
							K Value: 0.029713		4.468654

Lattice Parameters are in Angstroms

Ta2C	2Theta	Radians	D Spacing	ICDD	h	k	l	1+2	a	c	c/a
33.1	0.577704	2.704141	100	1	0	0	1.333333	3.122474			
36.1	0.630064	2.486003	002	0	0	2	1.598259		4.972005		
37.9	0.66148	2.371969	011	0	1	1	1.732898				
50	0.872665	1.822638	102	1	0	2	2.931592				
66.38	1.15855	1.407117	103	1	0	3	4.929415				
69.9	1.219985	1.344618	200	2	0	0	5.333333	3.105263			
71.42	1.246514	1.319689	112	1	1	2	5.598259				
							Average	3.113868	4.972005	1.596729	

Appendix 7-2 Lattice parameter example calculations for 19.8 at.% specimen. The peak data gathered by the XRD machine was analyzed by Origins software. Double peaks were de-convoluted. Example for TaC lattice parameter a- and Ta₂C lattice parameter a- and c- calculations are shown.

2Theta	Radians	D Spacing	Intensity	Normalization	TaC	Ta2C	Ta4C3
33.1	0.577704	2.704141	39.28003	0.053018284		100	
34.68	0.60528	2.584474	740.877	1	111		111
36.1	0.630064	2.486003	37.6378	0.050801686		002	
37.9	0.66148	2.371969	122.5295	0.165384406		011	
40.3	0.703368	2.236072	554.0748	0.747863415	200		200
50	0.872665	1.822638	24.79236	0.033463527		102	211
58.52	1.021367	1.575945	311.1641	0.419994254	220		220
66.38	1.15855	1.407117	31.37201	0.042344428		103	
69.9	1.219985	1.344618	428.1087	0.577840534	311	200	311
71.42	1.246514	1.319689	53.15347	0.071743985		112	
73.44	1.28177	1.288298	141.7384	0.191311726	222		
87.46	1.526465	1.114312	69.72844	0.094116086	400		
95.28	1.66295	1.042432	28.75918	0.03881775			
97.76	1.706234	1.022495	180.4289	0.243534204	331		
101.14	1.765226	0.997254	220.8664	0.298114767	420		
105.26	1.837134	0.969232	24.90461	0.033615037			421
112.1	1.956514	0.928579	33.29618	0.04494158			
115.82	2.02144	0.909191	184.2056	0.248631853	422		
118.06	2.060536	0.898352	26.4593	0.035713489			

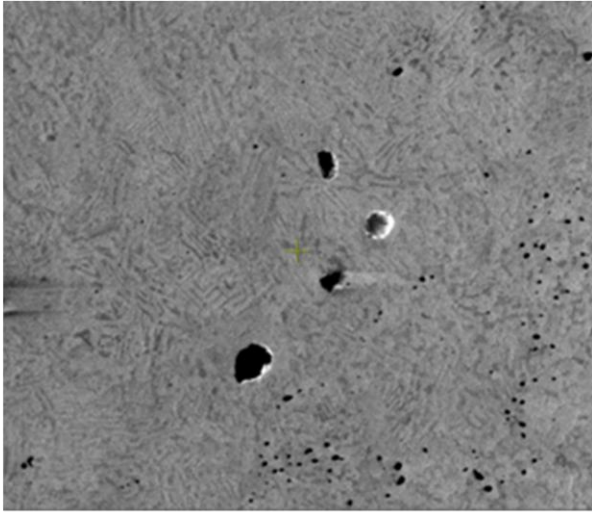
Peak data from peak analyzing software: Origins

Origins Software able to de-convolute double peaks

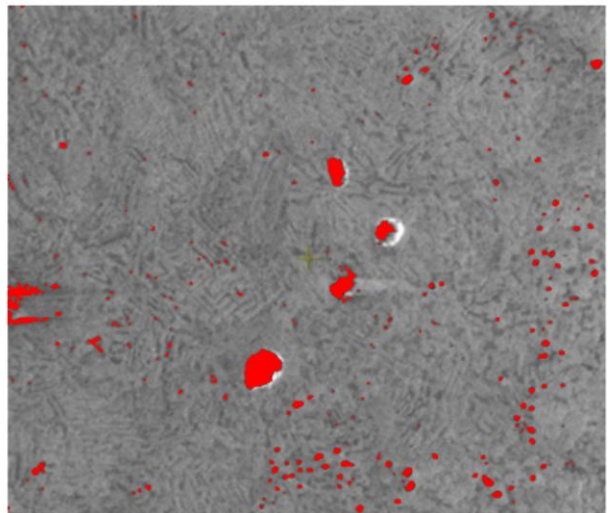
Phase	Orientation	Angle	Radians	D Spacing	Area	%	Phase %
TaC	[111]	34.9661	0.610274	2.563979	69.42234	30.74465	87.07774
Ta2C	[101]	38.15775	0.665978	2.356537	8.46968	3.750916	10.62368
Ta4C3	[107]	39.24743	0.684997	2.293582	1.83253	0.811562	2.298577

Appendix 7-3 Phase volume % example calculation for 19.8 at.% specimen. The peak data gathered by the XRD machine was analyzed by Origins software. Double peaks were de-convoluted. The most intense peak for each phase [111], [101], and [107] were used to calculate the phase %. The phase volume % was based off the area under the intense peak for each phase.

Initial SEM Image



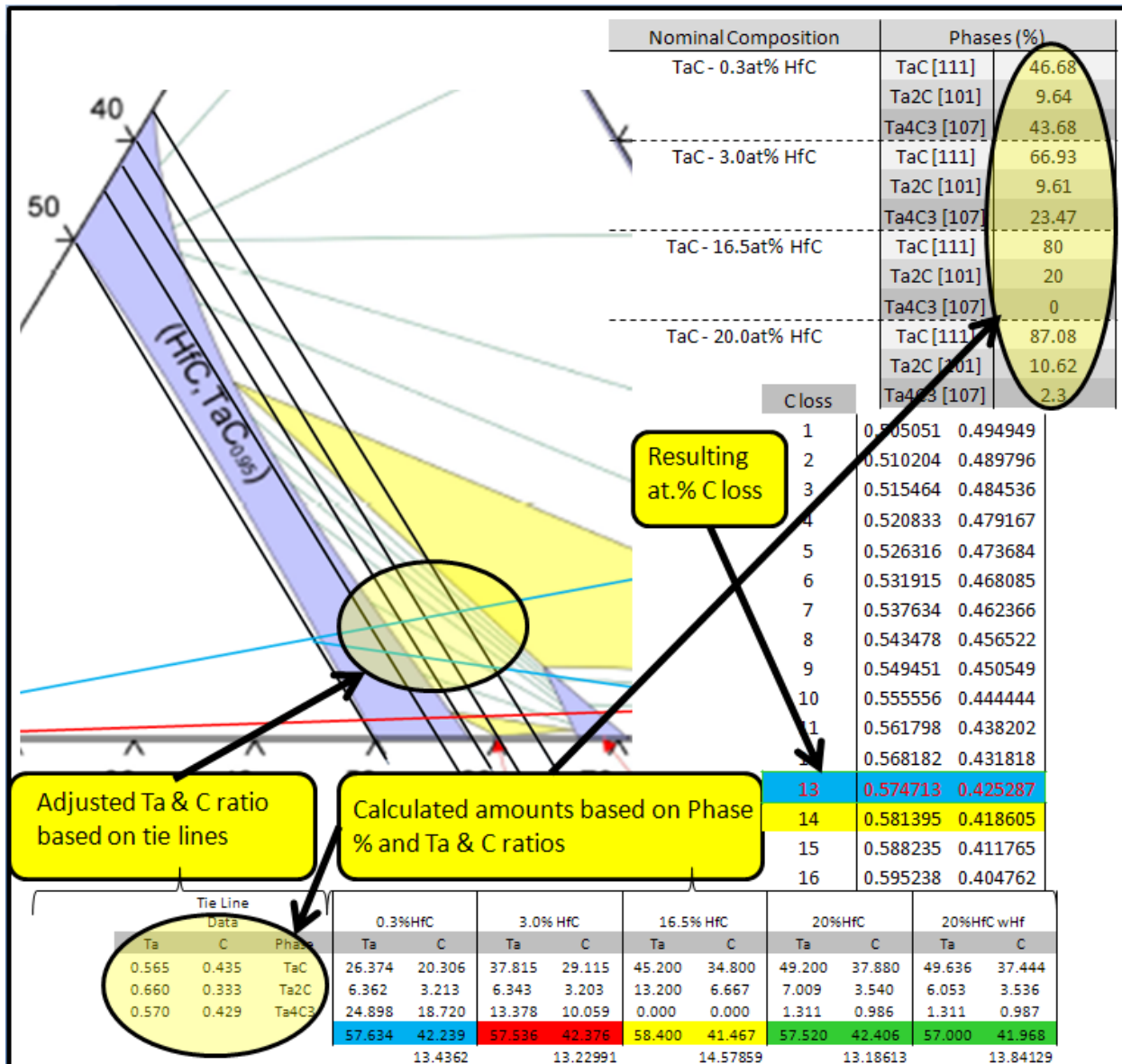
SEM Image with Threshold



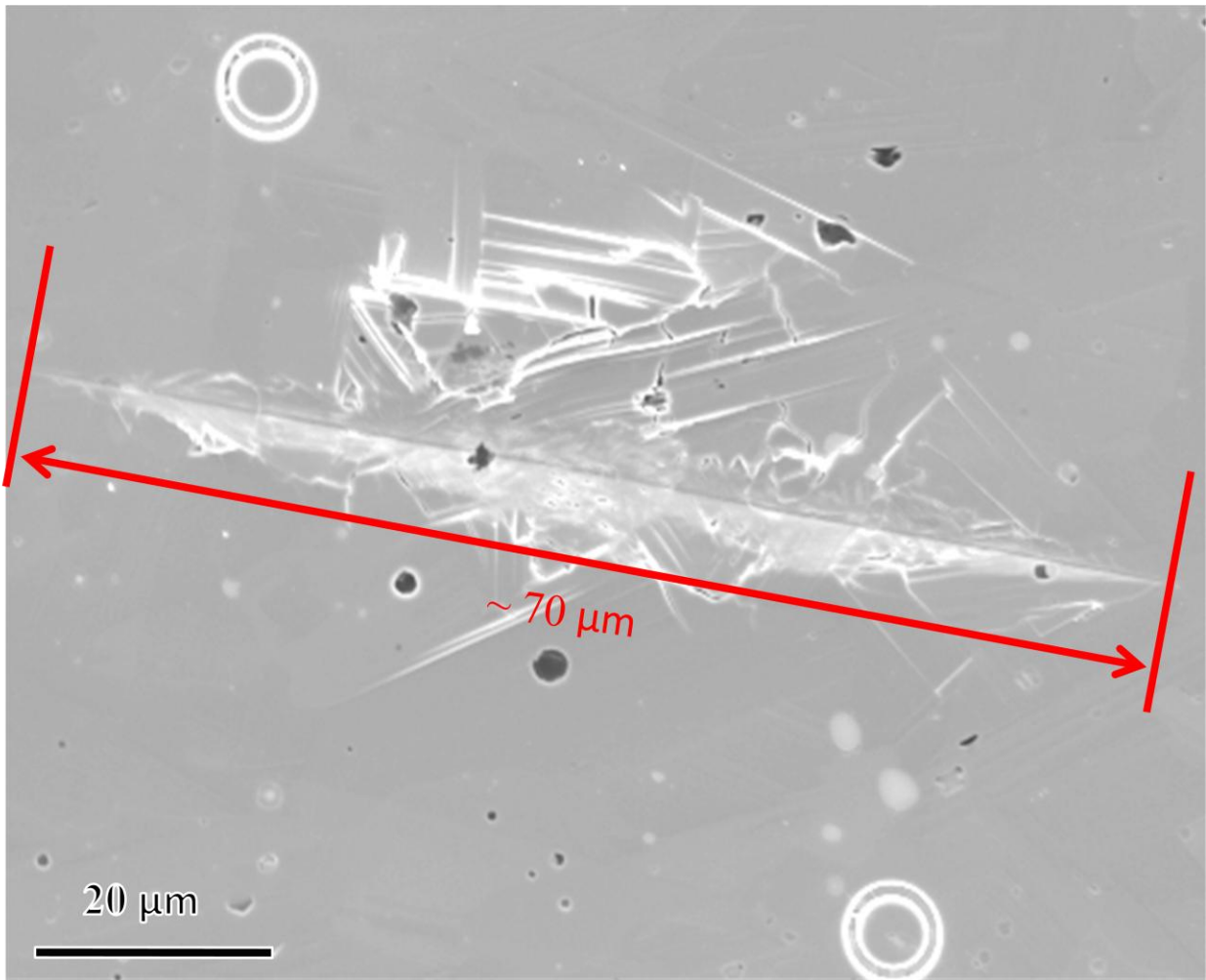
Threshold defined by R-G-B color scale

$$Porosity \% = 100 \times \frac{\text{Surface area of pores}}{\text{Total surface area}}$$

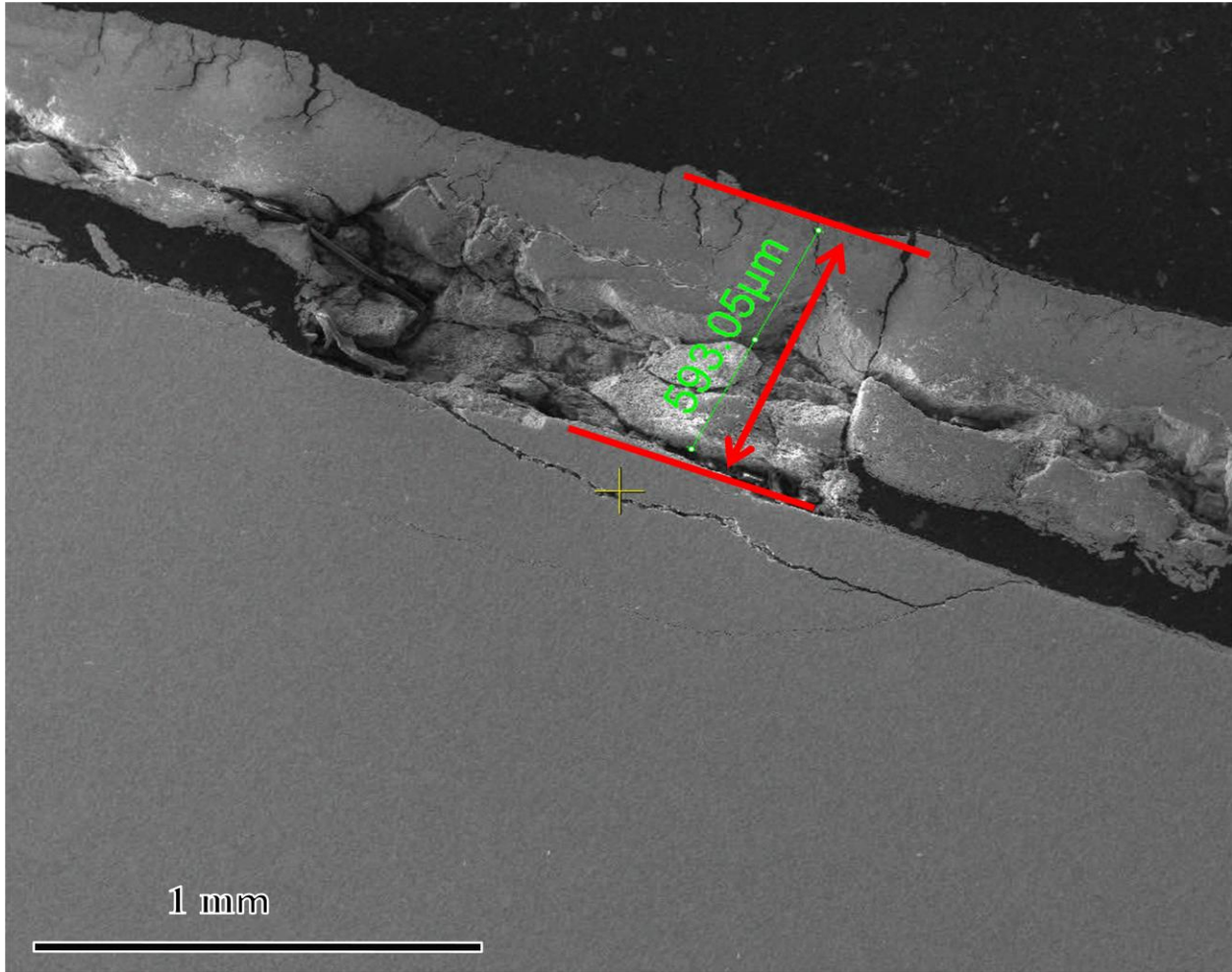
Appendix 7-4 Example porosity calculation. A generic SEM image would be analyzed with imaging software. A R-G-B color scale threshold was applied so that the dark regions (pores) were highlighted. The area of the pores was calculated by the software. The porosity % was calculated by the equation given.



Appendix 7-5 Sample at.% loss of carbon for the given phase diagram at 1850°C. Tie lines were measured in the region of interest for each specimen and the TaC boundary was adjusted for at.% of carbon at the tie line interface. These adjusted Ta and C values combined with phase % values produced a Ta:C ratio. This Ta:C ratio was used to determine the resulting overall at.% C loss for the specimen.



Appendix 7-6 Example Knoop indentation measurement. The length of the indentation at specified loads would correlate with a HK value.



ID	mol%	Pre HT	Mass (g)		Scale Thickness (μm)
			Post HT	% Change	SEM Measurements
21	6	2.058	2.109	2.496	593.05
22	11	1.702	1.738	2.167	359.16
23	18	4.061	4.128	1.647	198.16
24	25.5	1.923	1.934	0.596	106.94

Appendix 7-7 Example oxide mass % change and oxide scale thickness calculation. The mass % change was based on heat treated specimens loaded in ceramic boats which were normalized in the calculations. The mass of the boat and sample was measured before and after heat treatments to produce the mass % change. SEM images were used to measure the scale thickness. And average of 3 runs for both the mass change and scale thickness were conducted.